

Rochester Institute of Technology

RIT Digital Institutional Repository

Theses

12-2016

Effect of Transmission Line Measurement (TLM) Geometry on Specific Contact Resistivity Determination

Sidhant Grover
sxo1514@rit.edu

Follow this and additional works at: <https://repository.rit.edu/theses>

Recommended Citation

Grover, Sidhant, "Effect of Transmission Line Measurement (TLM) Geometry on Specific Contact Resistivity Determination" (2016). Thesis. Rochester Institute of Technology. Accessed from

This Thesis is brought to you for free and open access by the RIT Libraries. For more information, please contact repository@rit.edu.

Effect of Transmission Line Measurement (TLM) Geometry on Specific Contact Resistivity Determination

By

Sidhant Grover

A thesis submitted in partial fulfillment of the
requirements for the degree of
Master of Science in Materials Science and Engineering in the
School of Chemistry and Materials Science,
College of Science
Rochester Institute of Technology

December 2016

Signature of the Author _____

Accepted by _____
Director, MSE Degree Program Date

SCHOOL OF CHEMISTRY AND MATERIALS SCIENCE
COLLEGE OF SCIENCE
ROCHESTER INSTITUTE OF TECHNOLOGY
ROCHESTER, NEW YORK

CERTIFICATE OF APPROVAL

M.S. DEGREE DISSERTATION

The M.S. Degree Dissertation of Sidhant Grover has been examined and approved by the dissertation committee as satisfactory for the dissertation required for the M.S. degree in Materials Science and Engineering.

_____ Date: _____
Dr. Santosh Kurinec, *Thesis Advisor*

_____ Date: _____
Dr. Michael Jackson, *Committee Member*

_____ Date: _____
Dr. Robert Pearson, *Committee Member*

_____ Date: _____
Dr. Sean Rommel, *Committee Member*

Dedication

To my family, friends and fraternity brothers. For being a constant source of motivation and inspiring me to strive to be the best person I could possibly be.

Acknowledgments

Before anyone else, I would like to extend my sincerest gratitude to my advisor Dr. Santosh Kurinec for her continuous guidance throughout my senior project and masters thesis. Her constant support, motivation and encouragement has been invaluable throughout my research. I would like to thank her, not only for widening my research acumen but also for inspiring conversation about professional as well as personal development.

My sincere thanks also goes to Dr. Peng Zhang from Michigan State University for carrying out simulations for this work. His research and guidance on contact resistance modeling during his time at the University of Michigan has been tremendously helpful for this work. I would like to acknowledge Dr. Andrew Gabor from BrightSpot Automation LLC., for giving us access to their data and collaborating with us. I am also very grateful for Jim Carroll of PhotoMask PORTAL Inc. for their assistance with mask design and delivering it in a timely manner.

I would like to thank the rest of my committee Dr. Robert Person, Dr. Sean Rommel and Dr. Michael Jackson for their constant support and flexibility over the course of my thesis project work. I would also like to thank the SMFL staff, for their tremendous job in managing the cleanroom tools and assisting with tool training and certifications.

Abstract

Effect of Transmission Line Measurement (TLM) Geometry on Specific Contact Resistivity Determination

Sidhant Grover

Supervising Professor: Dr. Santosh Kurinec

Ohmic metal semiconductor contacts are indispensable part of a semiconductor device. These are characterized by their specific contact resistivity (ρ_c) in expressed in $\Omega\text{-cm}^2$, defined as the inverse slope of current density versus voltage curve at origin. Engineering and measurement of specific contact resistivity (ρ_c) is becoming of increasing importance in the semiconductor industry. Devices ranging from integrated circuits to solar cells use contact resistivity as a measure of device performance. Novel methods such as contact silicidation, doped-metal contacts, dipole inserted contacts etc. are continually being developed to reduce specific contact resistivity and improve device performance. The Transmission Line Measurement (TLM) method is most commonly used to extract the specific contact resistivity for such applications. This method is, however, not fully understood and modeled to understand the flow of current and behavior of charge carriers for contacts of different dimensions. It has often been observed in literature that applications that involve smaller TLM geometries most often than not, show low values of ρ_c and applications that involve ρ_c extraction through larger TLM geometries show significantly larger values. A perfect example of this would be the inconsistencies observed in extracted ρ_c 's from integrated

circuit applications where TLM geometries range from $0.1 \mu\text{m}$ to $10 \mu\text{m}$ and extracted ρ_c is of the order of 10^{-8} to $10^{-6} \Omega\text{-cm}^2$ and photovoltaic applications where geometries are around $50 \mu\text{m}$ to $1000 \mu\text{m}$ and ρ_c is of the order of 10^{-5} to $10^{-2} \Omega\text{-cm}^2$. The transfer length or L_T which is the characteristic length that the charge carriers travel beneath the contact before flowing up into the contact. It has also been seen that in certain cases of TLM device dimensions, the extracted L_T is greater than the actual length of the contact. This occurrence cannot be effectively explained through the conventional TLM analysis.

In this project, the inconsistencies observed in literature were initially attributed to the error in measurement. Equations for relative uncertainty due to systematic error were optimized to obtain values of optimum TLM widths for application specific values of ρ_c and R_{SH} . TLM structures with varying widths were fabricated and tested. Underlying doped regions were created through methods of ion implantation and spin-on-doping targeted for particular values of R_{SH} . The contacts were fabricated on high and low values of sheet resistances using Aluminum, NiSi and TiSi₂ metals. This was used to experimentally compare the experimental and simulated values of the optimum widths. The devices were also fabricated with changing contact length in order to try to explain the occurrence of the transfer length to be greater than the length of the contact. The experimental mask design had test structures with constant width and varying TLM lengths. Scaling structures where both the length and width of the TLM geometry were also increased proportionally to evaluate the scaling effect of the TLM length and width on the extracted transfer length.

The fabricated TLM structures were then tested and the data was analysed to obtain values of the transfer length (L_T) and ρ_c . The relative uncertainty due to systematic error in ρ_c was also evaluated. The experimental values of the optimum widths for the least amount of measurement error were a close match to those obtained through simulations. It was also observed that for a contact made with a particular metal on a doped layer of a particular R_{SH} , the L_T increased as the width of the TLM structure increased. Many

cases were observed where the extracted L_T was greater than the length of the contact, indicative of current crowding. This was the first time this relation was observed and this prompted a mask design with changing TLM lengths. A similar linear relation was observed on constant width and changing the length of the contacts. The scaled structures showed that on simultaneously increasing the length and width of the TLM contacts, the transfer length proportionally increased. There is, therefore, a geometric dependence of L_T extracted from the measurement of the TLM structures. Through the use of the exact field solution modeling, L_T is underestimated in the integrated circuit application space due to current crowding effects and overestimated in the case of silicon photovoltaics. There is no "one-size-fits-all" geometry that can be used for any particular application space. Due to the observed underestimations, it was also concluded that the TLM method is not an appropriate method to determine ρ_c for nanoscale contact applications.

Contents

Dedication	iii
Acknowledgments	iv
Abstract	v
1 Introduction	1
1.1 Motivation	3
1.2 Thesis Outline	6
2 Specific Contact Resistivity of Metal-Semiconductor Contacts	7
2.1 Ohmic Contacts	7
2.1.1 Schottky Barrier Height	8
2.1.2 Conduction Mechanisms	9
2.2 Specific Contact Resistivity	12
2.3 Effect of Interface States	15
2.4 Measurement Techniques	17
2.4.1 Cross Bridge Kevin Resistance (CBKR)	17
2.4.2 Shockley Method	18
3 Metal-Semiconductor Contact Technology	20
3.1 Aluminum Contact Technology	20
3.2 Metal-Silicide Contact Technology	22
3.2.1 Formation of Silicides	23
3.2.2 Self-aligned Silicide (SALICIDE)	24
4 Transmission Line Measurement (TLM) Method	32
4.1 Transmission Line Measurement (TLM) Structure	32
4.2 ρ_c Extraction	34

5	Contact Resistance Modeling	38
5.1	Three-Dimensional Model	39
5.2	Two-Dimensional Model	40
5.3	One-Dimensional Model	41
5.4	Zero-Dimensional Model	42
5.5	Lumped Circuit Model	42
5.6	Exact Field Solution Model	46
5.6.1	Changing Contact Resistivity of Interfacial Layer	49
5.6.2	Changing Contact Length	50
5.6.3	Changing Contact Height	52
6	Fabrication of TLM Structures	54
6.1	Implant Schemes for Target R_{SH}	56
6.2	Aluminum TLM Process Flow	58
6.3	NiSi TLM Process Flow	58
6.4	TiSi ₂ TLM Process Flow	59
6.5	Testing of Fabricated TLM Structures	59
7	TLM Structure Optimization	62
7.1	Optimization Through Error Analysis	62
8	Results and Discussion	68
8.1	Optimization Results	68
8.2	TLM Width and Transfer Length	73
8.3	TLM Design Length and Transfer Length	74
8.4	TLM Scaling	75
8.5	Modeling Results	76
8.5.1	Fourier Series Analysis Modeling	77
9	Conclusions and Future Work	81
9.1	Conclusions	81
9.2	Future Work	82
	Bibliography	84
A	Detailed Process Flow	87

B ATHENA code for Implant Simulations 93

List of Tables

2.1	Schottky barrier height and work function of a few different metals [13].	9
3.1	Main properties of common silicides [3].	22
5.1	Recalculation of ρ_c from general formula.	46
6.1	Dose and Energy implant parameters for target values of R_{SH}	57

List of Figures

1.1	Transmission lines and the TLM circuit model [2]	2
1.2	Example of a TLM structure	2
1.3	Difference of ρ_c values in literature between Integrated Circuits and Silicon Photovoltaics.[5] [6] [7] [16]	4
1.4	Map of optimum widths for different applications 1 and 2.	5
2.1	Energy band diagram of Metal-Semiconductor contact in thermal equilib- rium.	8
2.2	Current conduction in Metal-Semiconductor junctions.	10
2.3	E_{00} and kT as a function of doping density for Si at T = 300K [15].	11
2.4	Electron concentration versus specific contact resistivity for Silicon.	14
2.5	Energy levels of interface states	15
2.6	Metal workfunction as a function of barrier height.	16
2.7	Structure used for CBKR measurement[18].	17
2.8	Ladder-structure contacts on doped-semiconductor region, top-down view.	19
2.9	Extraction of the transfer length using the Shockley method	19
3.1	Al/Si phase diagram [21].	21
3.2	Pit formation and junction spiking [13].	22
3.3	Multiphases in Ti/Si sample [3].	24
3.4	SALICIDE on MOSFET source/drain [3].	25
3.5	Description of SALICIDE process[17].	26
3.6	Ti-Si equilibrium binary phase diagram [12].	27
3.7	Resistance versus temperature curve for <i>in situ</i> annealing of Ti/poly-Si [11].	28
3.8	SALICIDE process window for reduced linewidth and film thickness [11].	29
3.9	Ni/Si phase diagram [19].	30
3.10	Film resistivity versus annealing temperature for NiSi [4].	30
4.1	Top-down view of TLM structure.	33
4.2	Horizontal view of TLM device structure.	33

4.3	Plot to extract transfer length from the TLM method.	34
4.4	Current path under metal contact to n-type semiconductor.	35
4.5	Current flow into the contact for low and high ρ_c	35
4.6	Transfer length as a function of ρ_c	36
5.1	Non-uniform current distribution in a contact.	38
5.2	Resistive network for metal-semiconductor contact resistance [8].	43
5.3	Voltage distribution under contact [8].	43
5.4	Coth function	45
5.5	Electrical contact assumed for Finite Element Model [24].	47
5.6	Two contact model for the Exact Field Solution Model.	48
5.7	(a) Current density distribution on changing ρ_c from the exact field solution model. (b) Transfer length as a function of interfacial contact resistivity (ρ_c) [25].	50
5.8	(a) Current density distribution on changing contact length (a) from the exact field solution model. (b) Transfer length as a function of contact length, $a(\mu\text{m})$ [25].	51
5.9	(a) Current density distribution on changing conducting layer (h_2) from the exact field solution model. (b) Transfer length as a function of height of conducting layer (h_2) [25].	53
6.1	Mask layout for constant TLM length and different widths.	55
6.2	Mask layout for constant TLM width and different lengths.	55
6.3	TLM fabrication process flow.	56
6.4	Aluminum TLM formation	59
6.5	Testing of TLM structures	60
6.6	I-V plots obtained from measuring resistive contacts from different spacings in the TLM test structure.	60
7.1	Depiction of systematic error through δR or δd on ρ_c extraction through the TLM method [20].	65
7.2	Contour map of W_{opt} for application specific ρ_c and R_{SH}	67
8.1	Contour plot of the systematic error optimization for application specific values of ρ_c and R_{SH}	69
8.2	Relative uncertainty due to systematic error as a function of TLM width for (a) low and (b) high R_{SH} using Al and NiSi contact metals.	70

8.3	Relative uncertainty due to systematic error in specific contact resistivity (ρ_c) as a function of TLM length (L, μm) for $R_{SH} = 1000 \Omega$ and $W = 100\mu\text{m}$.	71
8.4	Relative uncertainty due to systematic error in specific contact resistivity (ρ_c) as a function of TLM length (L, μm) for $R_{SH} = 50 \Omega$ and constant width $W = 100\mu\text{m}$.	71
8.5	Relative uncertainty due to systematic error in specific contact resistivity (ρ_c) as a function of TLM length (L, μm) for $R_{SH} = 10 \Omega$.	72
8.6	Transfer Length as a function of TLM width (W, μm).	73
8.7	Dependence of transfer length on the length of TLM at constant width.	74
8.8	Scaled TLM contact structures with 1x, 2x and 4x scaling.	75
8.9	Scaling effect of TLM dimensions on Transfer Length.	76
8.10	Two contact structure for Fourier Series Analysis simulations.	77
8.11	Modeled transfer length versus specific contact resistivity for $a = 10\mu\text{m}$.	78
8.12	Modeled transfer length versus specific contact resistivity for $a = 100\mu\text{m}$.	79
9.1	Overestimation and Underestimation by the TLM model.	83

Chapter 1

Introduction

The advent of modern technological society can be largely attributed to tremendous developments in the semiconductor industry in the past 50 years. Breakthroughs in fabricating smaller and faster integrated circuits as well as more efficient solar cells has created a well connected and environment friendly world around us. The need to improve the performance of these advanced semiconductor devices is what drives a majority of technological advancements today.

Device performance in the semiconductor industry can be impacted by various means. One of the major factors that effect the performance of devices is the resistance between the contacts and the device itself. This is termed as contact resistance. This contact resistance is dependent on contact area. Therefore, a more critical figure of merit called the specific contact resistivity can be employed. The Specific Contact Resistivity or ρ_c is a more effective characteristic as it is independent of contact area size and is a convenient factor while comparing contacts of different sizes. The Transmission Line Method (TLM) can be applied to extract the ρ_c of these contacts. This model gains its name from transmission lines that are used in power transmission. The initial circuit model was based on how transmission lines looked like in the last century as seen in Figure 1.1.

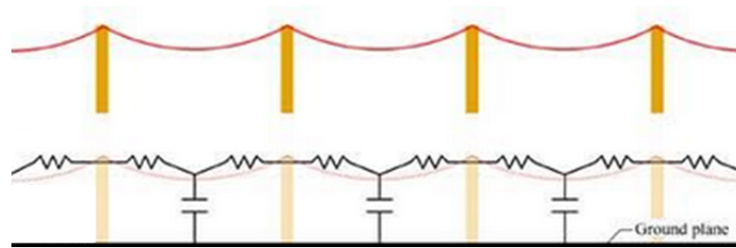


Figure 1.1: Transmission lines and the TLM circuit model [2]

The TLM test structures involve metal contacts fabricated on diffused conducting regions. These contacts have a particular length (L) and width (W) and different spacings between them. Figure 1.2 shows an example of a sample TLM structure. The MESA region is the diffused conducting region. Electrical testing on these structures (described in further detail in Chapter 4) is used to extract the ρ_c .

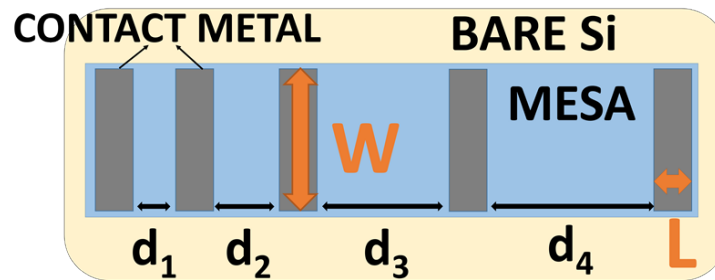


Figure 1.2: Example of a TLM structure

Accurate determination of this ρ_c is essential in understanding its impact on the performance of these devices. This chapter provides a description of the motivation behind this work, a brief overview of TLM analysis and need for optimization. It lays out an outline for the rest of the work and motivates further reading.

1.1 Motivation

The aggressive demand for high performance semiconductor devices has placed a need to effectively extract the specific contact resistivity for contacts made between these devices and their external environment. Integrated circuits and photovoltaic applications commonly use the Transmission Line Method or TLM method to extract the measure of contact resistance i.e. specific contact resistivity or ρ_c . In the TLM method, the contact current injection is in a lateral channel that makes the extracted specific contact resistivity values comparable to FET as well as photovoltaic devices. These device structures have varying ρ_c and sheet resistance R_{SH} values and the contacts differ between being alloyed and non-alloyed metal contacts.

Inconsistencies have been observed in literature regarding the specific contact resistivity values extracted from applications involving large TLM geometries and small TLM geometries. For example, values of ρ_c quoted in literature involving integrated circuit applications that have very small TLM contact geometries range from about 10^{-8} to 10^{-6} $\Omega - cm^2$ [7] [16] whereas those in the photovoltaics domain with larger contact geometries have values of ρ_c between 10^{-5} to 10^{-2} $\Omega - cm^2$ [6] [5]. This is very interesting to observe as ρ_c is defined to be independent of contact area, but an area dependence is clearly observed in such literature.

An extensive literature search was carried out to compare various ρ_c values found in literature for particular TLM dimensions. It was interestingly noted that not all of the papers studied investigated mentioned TLM dimensions that were used for the measurements. Figure 1.3 shows a TLM Geometry versus ρ_c space with various data values listed illustrating how varied the results have been reported. The differences in measured values of ρ_c due to application specific dimensional variation can clearly be identified.

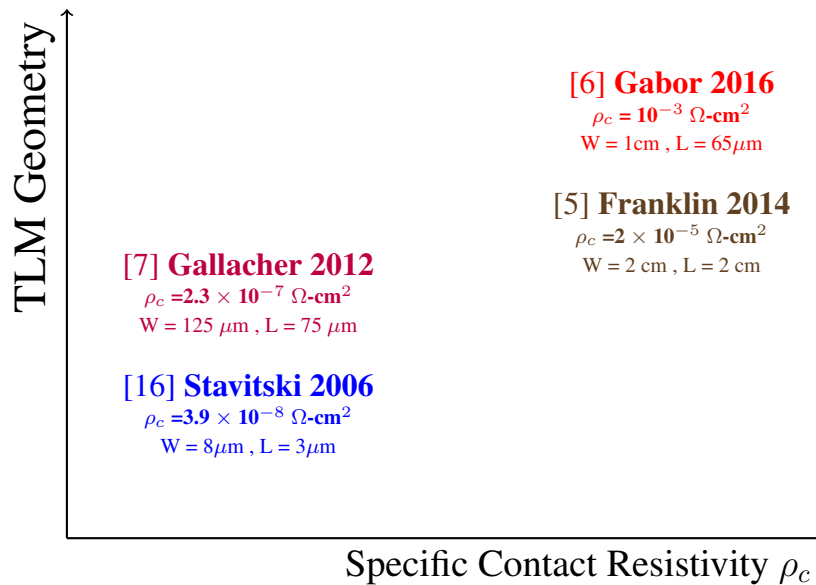


Figure 1.3: Difference of ρ_c values in literature between Integrated Circuits and Silicon Photovoltaics.[5] [6] [7] [16]

Tremendous reduction in device sizes in modern times have required specific contact resistivity (ρ_c) improvement to maintain small parasitic resistances within acceptable ranges, particularly for integrated circuit applications. These parasitic resistances need to be significantly small for all semiconductor applications. Optimum pattern designs for the Transmission Line Model (TLM) that are suggested to achieve minimum measurement uncertainty of the specific contact resistance can be developed for semiconductor applications of varying ρ_c and R_{SH} . These values of measurement uncertainty need to be evaluated for TLM geometries of varying sizes to determine if non-optimized TLM geometries cause the measurement inconsistencies. Simulations carried out in this paper as well as in Ueng et al [20] suggest optimum values of the widths of these TLM structures that provide the least uncertainty in measurement. A contour map similar to one below can be formulated for optimum TLM contact geometries for various values of R_{SH} and ρ_c yielding to different semiconductor applications.

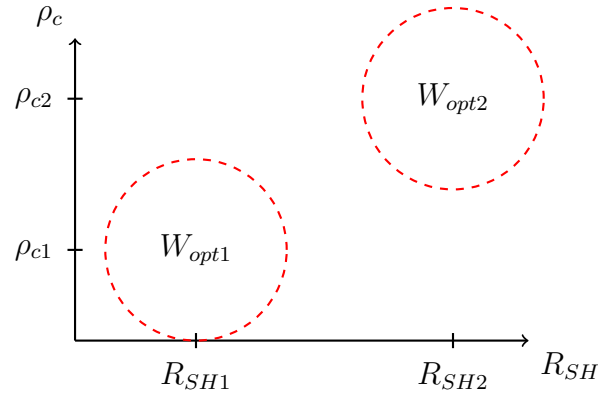


Figure 1.4: Map of optimum widths for different applications 1 and 2.

Figure 1.4 shows a map of the different optimum widths of TLM structures for applications 1 and 2 with values of sheet resistances R_{SH1} and R_{SH2} , and specific contact resistivities ρ_{c1} and ρ_{c2} . There is no information on the uncertainties of these alloyed and non-alloyed structures and hence one cannot accurately compare data sets. Similar issues arise for different applications employing varying values of R_{SH} and ρ_c .

The Transmission Line Measurement or TLM method involves current-voltage measurements on contacts of particular dimensions fabricated on diffused resistors of different doping. These contacts have varying spacing between them and the resistance is measured between each contact of different spacing. The measured resistance is then plotted with the different spacings and the plot is used to extract parameters of transfer length (L_T) and specific contact resistivity (ρ_c). The transfer length is an important factor in the determination of the specific contact resistivity and is defined as the characteristic length along which 63% of the current flows into the contact. Conventional TLM structures do not accurately determine the L_T of the contact. Lateral contacts that have contact lengths much larger than L_T behave as semi-infinite contacts. As the length of the contacts is decreased, below L_T , the resistance of the contact increases sharply [14]. The assistance of different modeling methods such as Exact Field Solutions, Lumped circuit modeling, dimensional modeling

using the Finite Element Method can be used to explore reasons for such dependencies.

1.2 Thesis Outline

This work follows a logical order starting with the definition of specific contact resistivity of metal-semiconductor contacts. By talking about the Schottky barrier height, the various conduction mechanisms in Metal-Semiconductor ohmic contacts can be discussed and their relationship to the specific contact resistivity can be shown. The technology and operation of metal-semiconductor contact formation techniques like aluminum-to-silicon contacts and silicided contacts is provided. The Transmission Line Measurement (TLM) method is then described in detail and different modeling methods such as the three, two, one and zero dimensional models, the lumped circuit model and the exact field solution model are described.

The process fabrication and experiment and then outlined followed by details of the theoretical and experimental optimization carried out through error analysis. The results of the modeling and optimization, the impact of changing the TLM dimensions on the transfer length are then provided. The experimental measurement errors are also analyzed in the above results. The above results are then summarized to provide conclusions about the applicability of the TLM method as an accurate method for determining ρ_c and ideas for improvement and future research are suggested.

Chapter 2

Specific Contact Resistivity of Metal-Semiconductor Contacts

2.1 Ohmic Contacts

In order to improve the performance of modern semiconductor devices, various methodologies can be applied. One of them is to reduce the resistance between the electrical contacts of the device and its environment. Ohmic contacts are most commonly utilized to make connections between the metal and semiconductors. An ohmic contact is a low resistance junction that allows similar current conduction in both directions between the metal and the semiconductor [22]. The current voltage characteristics of ohmic contacts can be linear or quasi-linear. The voltage drop across the contact junction should be very small when compared to the voltage drop across the device so that the contact can provide the necessary device current [15]. An ohmic contact should not degrade the device and inject minority carriers.

An essential concept to comprehend for ohmic contacts is the barrier height or more formally called the Schottky barrier height, denoted by ϕ_B and measured in eV.

2.1.1 Schottky Barrier Height

The barrier between a metal and semiconductor can be identified using an energy band diagram as shown in figure 2.1. The work function of the metal ϕ_M is the minimum energy required to raise an electron from the fermi level E_f to the vacuum level E_{vacuum} . The electron affinity χ is the difference in energy of an electron in the vacuum level and the conduction band edge. When the metal and semiconductor are brought in intimate contact, electrons travel from the semiconductor to the metal in order to achieve thermal equilibrium.

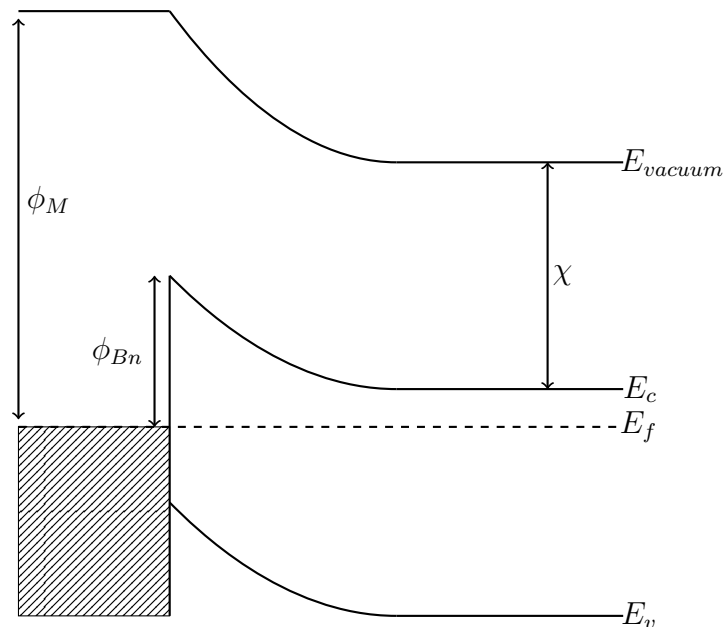


Figure 2.1: Energy band diagram of Metal-Semiconductor contact in thermal equilibrium.

In Figure 2.1, Fermi level, E_f is flat as no voltage is applied across the junction. The right of the junction is an n-type semiconductor and to the left of the junction is a metal. The Schottky barrier height is described as a barrier to the electron or hole flow between a metal and doped semiconductor. For an n-type semiconductor, it is given as ϕ_{Bn} and is the energy difference between the fermi energy of the metal and the band edge where the majority carriers reside [10]. For a p-type semiconductor it is ϕ_{Bp} and called ϕ_B in general.

It is a function of the metal as well as the semiconductor. The barrier height for a metal contact to an n-type semiconductor is given in Equation 2.1.

$$\phi_{Bn} = \phi_M - \chi \quad (2.1)$$

Here, ϕ_M is the metal work-function and χ is the electron affinity. Similarly, for a p-type semiconductor, the barrier height ϕ_{Bp} is given in Equation 2.2.

$$\Phi_{Bp} = \frac{E_g}{q} + \chi - \phi_M \quad (2.2)$$

where E_g is the band-gap of the semiconductor. Measured Schottky barrier heights for for electrons on n-type silicon and holes on p-type silicon for a few different metals is shown in Table 2.1.

Metal	ϕ_M (V)	n-Ge	p-Ge	n-Si	p-Si	n-GaAs	p-GaAs
Ag	4.3	0.54	0.5	0.78	0.54	0.88	0.63
Al	4.25	0.48		0.72	0.58	0.8	
Au	4.8	0.59	0.3	0.8	0.34	0.9	0.42
Cr	4.5			0.61	0.5		
Ni	4.5	0.9		0.61	0.51		
Pt	5.3			0.9		0.84	
W	4.6	0.48		0.67	0.45	0.8	

Table 2.1: Schottky barrier height and work function of a few different metals [13].

2.1.2 Conduction Mechanisms

Conduction in metal-semiconductor junctions can be described by three main mechanisms depending on the semiconductor doping. For low-doped semiconductors with a doping density $N_D < 10^{17} \text{ cm}^{-3}$, conduction is mainly through Thermionic emission (TE, Fig. 2.2a). For heavily doped semiconductors $N_D > 10^{19} \text{ cm}^{-3}$, Field Emission (FE) is the

major conduction mechanism where electrons tunnel through the barrier (Fig. 2.2b). For moderately doped semiconductors, the electrons are excited to energy levels where tunneling can take place and this mechanism is called Thermionic Field Emission (TFE, Fig 2.2c).

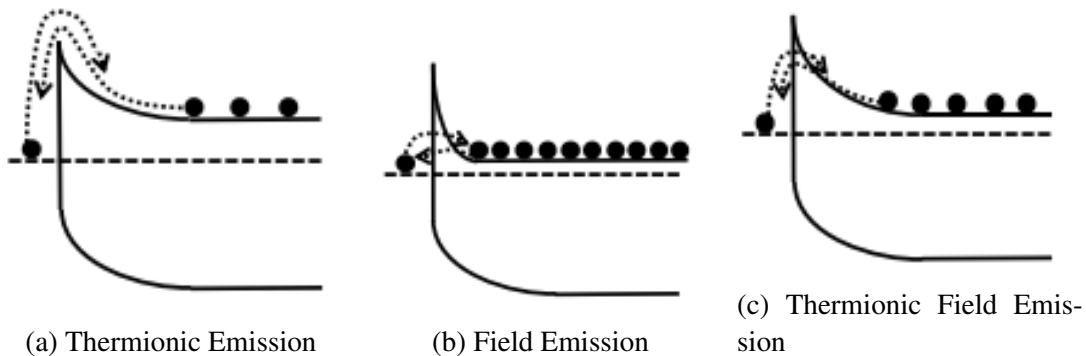


Figure 2.2: Current conduction in Metal-Semiconductor junctions.

The three different regimes are differentiated by considering the characteristic energy E_{00} that is given Equation 2.3.

$$E_{00} = \frac{qh}{4\pi} \sqrt{\frac{N}{\epsilon_s m^*}} = 1.86 \times 10^{-11} \sqrt{\frac{N(cm^{-3})}{\epsilon_s m^*}} \quad (2.3)$$

where N is the doping density, q is electron charge = 1.6×10^{-19} , ϵ_s is the relative permittivity of the material and m^* is the effective electron mass. E_{00} can be plotted with respect to the doping density and compared with the thermal voltage kT . For $kT \gg E_{00}$, Thermionic Emission dominates. Field Emission dominated for $kT \ll E_{00}$ and for $kT \approx E_{00}$, Thermionic-Field Emission dominates. This behavior can be observed in Figure 2.3.

The process of Thermionic Emission (TE) involves electrons being emitted over a barrier with thermal energies greater than that of the barrier. The current density obtained from this process is given by Equation 2.4.

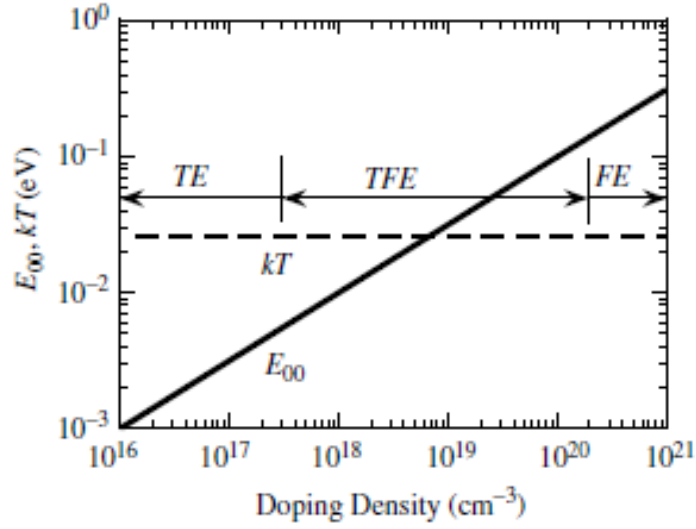


Figure 2.3: E_{00} and kT as a function of doping density for Si at $T = 300\text{K}$ [15].

$$J_{TE} = A^*T^2 \exp\left(\frac{-q\phi_B}{kT}\right) \left[\exp\left(\frac{qV}{kT} - 1\right) \right] \quad (2.4)$$

where A^* is called Richardson Constant and is given by Equation 2.5.

$$A^* = \frac{4\pi qmk^2}{h^3} \quad (2.5)$$

The current densities for Thermionic Field Emission (TFE) and Field Emission (FE) depend on the barrier height ϕ_B and doping. Their expressions are given by Equations 2.6 and 2.7.

$$J_{FE} = \frac{A^*T\pi \exp\left[\frac{-q(\phi_B - V)}{E_{00}}\right]}{c_1 k \sin(\pi c_1 kT)} \cdot [1 - \exp(c_1 qV)] \quad (2.6)$$

$$J_{TFE} = \frac{A^*T\sqrt{\pi E_{00}q(\phi_B + v_f - V)}}{k \cdot \cosh\left(\frac{E_{00}}{kT}\right)} \exp\left[\frac{q\phi_B}{kT} - \frac{q(\phi_B - v_f)}{E_0}\right] \exp\left(\frac{qV}{E_0}\right) \quad (2.7)$$

The variables c_1 and E_0 are defined as follows.

$$c_1 = \frac{1}{2E_{00}} \ln \left(\frac{4\phi_B}{v_f} \right) \quad (2.8)$$

$$E_0 = E_{00} \coth \left(\frac{E_{00}}{kT} \right) \quad (2.9)$$

v_f is the difference between E_c and E_f and can be found using the Joyce-Dixon approximation.

$$v_f = E_C - E_f = kT \left[\ln \left(\frac{n}{N_c} \right) + \frac{1}{\sqrt{8}} \frac{n}{N_c} \right] \quad (2.10)$$

where n is the carrier concentration and N_c is the effective density of states given by

$$N_c = 2 \left(\frac{m_e^* kT}{2\pi \hbar^2} \right)^{3/2} \quad (2.11)$$

m_e^* is the effective mass of electron and the value of N_c for silicon is $2.82 \times 10^{19} \text{cm}^{-3}$.

2.2 Specific Contact Resistivity

The specific contact resistivity, ρ_c , is a figure of merit for ohmic contacts and is measured in $\Omega \cdot \text{cm}^2$. It is used to describe the interfacial quality of the junction. The classic derivation of ρ_c is the reciprocal of the derivative of the current density with respect to the voltage at zero bias [17],

$$\rho_c = \left(\frac{\partial J}{\partial V} \right)_{V=0}^{-1} \quad (2.12)$$

The specific contact resistivity includes the contact resistivity of not only the interface,

but also the regions immediately above and below the interface. The specific contact resistivity is a very useful parameter for ohmic contacts as it is independent of the contact area and is a very convenient parameter for measuring contacts of different sizes. The ρ_c can be measured directly in contrast to contact resistance R_c . ρ_c can be measured from the corresponding R_c as

$$\rho_c = R_c A \quad (2.13)$$

where A is the effective contact area in cm^2 .

For metal-semiconductor contacts with low doping concentrations, Thermionic Emission dominates. The current due to TE is given by Equation 2.4. The specific contact resistivity due to TE can be obtained by applying Equation 2.12 to the TE current. Therefore, the specific contact resistivity due to Thermionic Emission

$$\rho_{c,TE} = \frac{k}{qA^*T} \exp\left(\frac{q\phi_B}{kT}\right) \quad (2.14)$$

It can be seen from the above equation that low ρ_c can be obtained from a low barrier height. It also shows the temperature dependence of the ρ_c for a given barrier height. For higher doping concentrations, ρ_c starts to depend on the barrier height ϕ_B as well as the doping density N_D . The specific contact resistivity due to Field emission, $\rho_{c,FE}$, is given by

$$\rho_{c,FE} = \frac{k^2}{qA^*} \cdot \frac{\sqrt{E_0}}{E_{00}\sqrt{\pi(q\phi_B + v_f)}} \cosh\left(\frac{E_{00}}{kT}\right) \exp\left(\frac{q\phi_B}{E_0} - \frac{v_f}{kT}\right) \quad (2.15)$$

For regions in between, both TE and FE take place the specific contact resistivity, $\rho_{c,TFE}$ is given by

$$\rho_{c,TFE} = \frac{k^2}{qA^*} \cdot \left[\frac{\pi kT}{\sin(\pi c_1 kT)} \cdot \exp\left(-\frac{q\phi_B}{E_{00}}\right) - \frac{1}{c_1} \exp\left(-\frac{q\phi_B}{E_{00}} - c_1 v_f\right) \right]^{-1} \quad (2.16)$$

The Richardson constant A^* for silicon is $110 \text{ Acm}^{-2}\text{K}^{-2}$.

The specific contact resistivity can be plotted with respect to the doping concentration to show its variation with different barrier heights as seen in Figure 2.4.

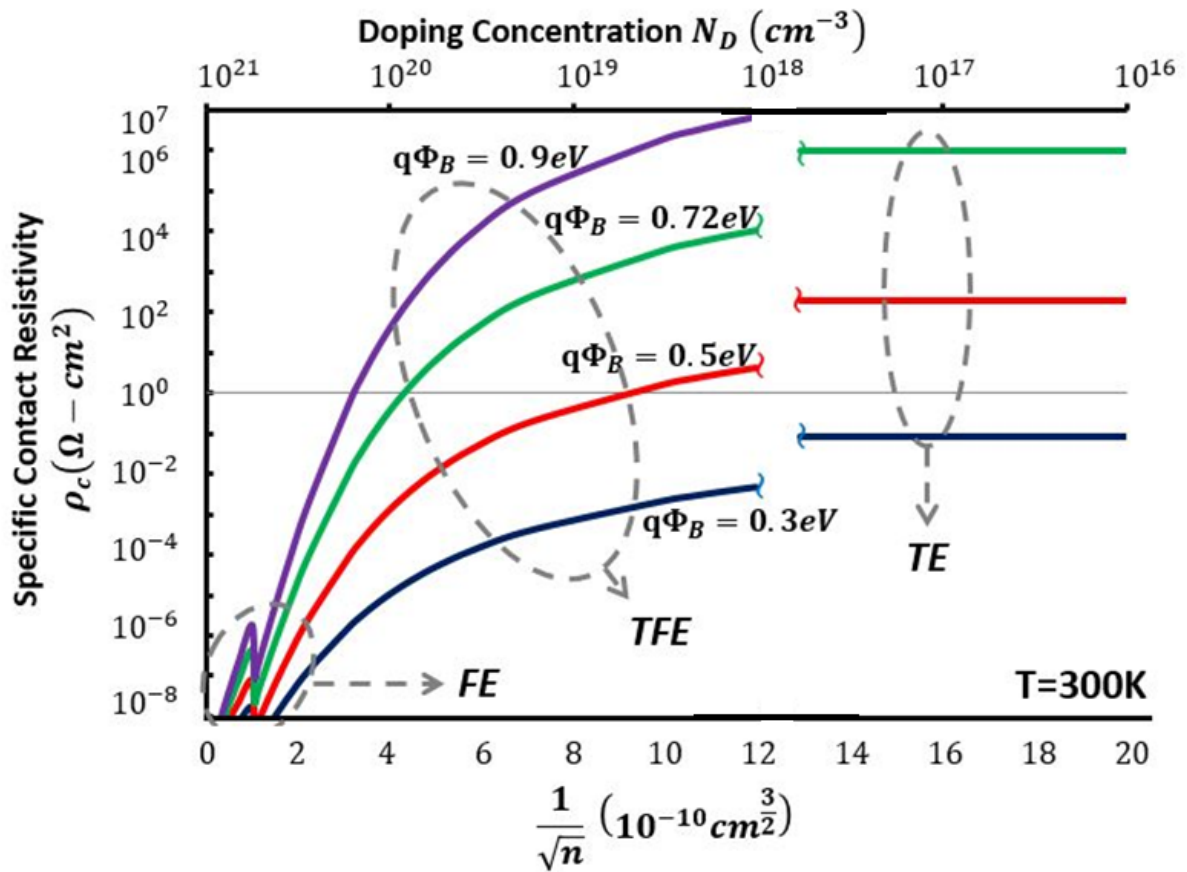


Figure 2.4: Electron concentration versus specific contact resistivity for Silicon.

It can be observed from the above graph that for higher doping concentrations, lower specific contact resistivity values can be obtained. The values of ρ_c are calculated for each of the conduction mechanisms using equations 2.14 through 2.16 respectively. It can be observed that Field Emission dominates as a transport mechanism in highly doping whereas Thermionic Emission dominates at low doping. The specific contact resistivity is independent of the doping in the Thermionic emission regime and therefore straight lines are

observed. The specific contact resistivity increases with increasing barrier height and therefore, lower barrier heights with high electron concentration are preferred. At low barrier heights, however, very less field emission is observed for high doping concentrations. A discontinuity is also observed in the regions of transition from one transport mechanism to the other.

2.3 Effect of Interface States

Interface states on the surface of the semiconductor can also be a significant factor in determining the specific contact resistivity. These interface states can be caused by various reasons such as broken lattice periodicity on the surface, adsorption of foreign particles and impurities. These can give rise to trap sites on the semiconductor surface. The trap sites can be of donor or acceptor type. The sites that are positive when empty and neutral when full are the donor-like trap sites and the ones that are neutral when empty and negative when full are the acceptor like trap sites.

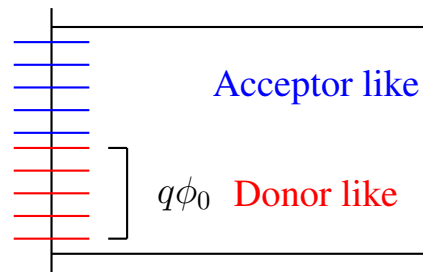


Figure 2.5: Energy levels of interface states

$q\phi_0$ is the neutral level. Above the neutral level, states are acceptor like and below it, states are donor like. The interface trap density is given as D_{it} and is measured in number of states/cm²-eV. ϕ_0 and D_{it} can be found using the equations below.

$$\phi_0 = \frac{E_g}{q} - \frac{c_3 + c_2\chi}{(1 - c_2)} \quad (2.17)$$

$$D_{it} = 1.1 \times 10^{13} \left(\frac{1 - c_2}{c_2} \right) \quad (2.18)$$

E_g is the band gap, χ is the electron affinity, c_2 and c_3 are constants. When there are no surface states present, $D_{it} \rightarrow 0$. Then, $c_2 \rightarrow 1$ which causes the barrier height to be a function of the metal-semiconductor workfunction difference forming an ideal schottky barrier. When the amount of surface states is large, $D_{it} \rightarrow \text{inf}$, then $c_2 \rightarrow 0$. In this case, $\phi_{Bn} = E_g - \phi_0$. The fermi-level is pinned to the surface states at a value $q\phi_0$ above the valence band. The barrier height is then independent of the metal workfunction and is determined entirely by the semiconductor surface properties. This phenomenon is also known as Fermi-level pinning. It shows the importance of semiconductor surface pre-cleaning prior to metal deposition in order to reduce the trap states between the metal-semiconductor interface. [15] [3]

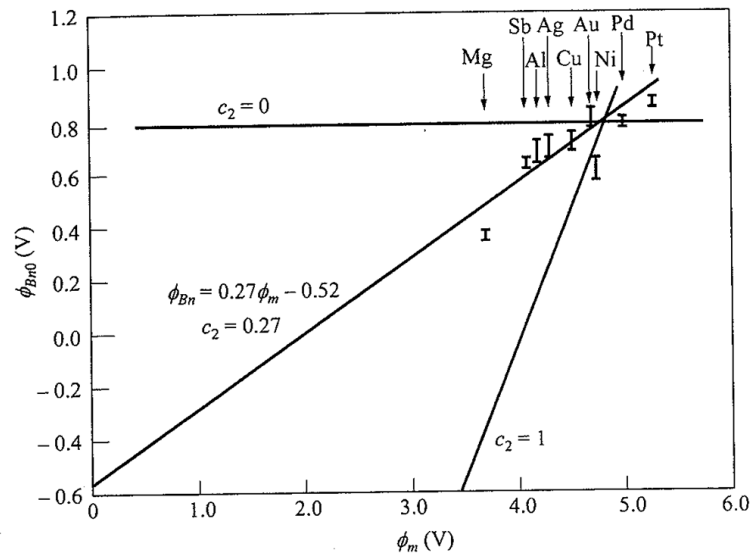


Figure 2.6: Metal workfunction as a function of barrier height.

2.4 Measurement Techniques

There are numerous methods ranging from two-contact two-terminal techniques to six-terminal methods to measure the specific contact resistivity, ρ_c . A few of the test structures commonly employed to measure ρ_c are discussed in this section with additional emphasis on ladder structures leading into the Transmission Line Measurement (TLM) method.

2.4.1 Cross Bridge Kevin Resistance (CBKR)

The Cross Bridge Kevin Resistor or CBKR is a popular four-terminal technique to measure the specific contact resistivity ρ_c for metal-to-semiconductor contacts.

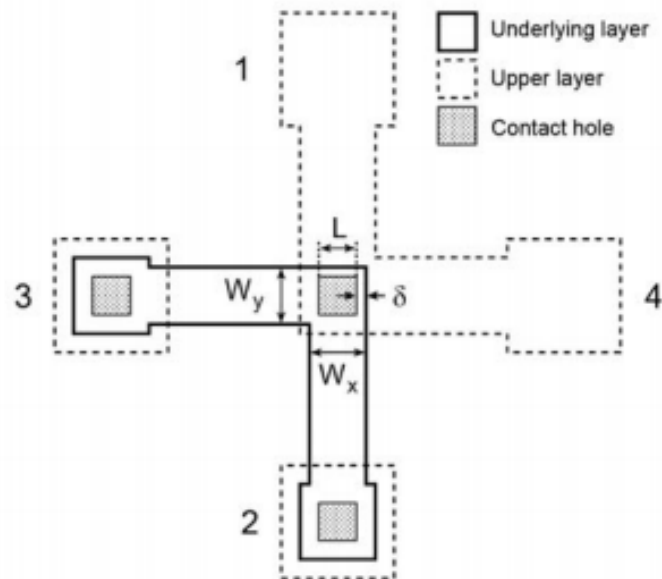


Figure 2.7: Structure used for CBKR measurement[18].

In the following method, a current I is forced between contacts 1 & 2 and the voltage drop is measured between contacts 3 & 4, $V_{3,4} = V_3 - V_4$. The underlying layer is the doped semiconductor region whereas the upper layer is the metal used for the contact. The value

of the contact resistance R_c is then given by Equation 2.19 below.

$$R_{CBKR} = \frac{V_{3,4}}{I} \quad (2.19)$$

The specific contact resistivity can then be calculated from the contact area, A , using the following equation where $R_{CBKR} = R_c$.

$$\rho_c = R_c A \quad (2.20)$$

This generic one-dimensional approach does not take into account the effects of current crowding that occur when the contact hole window is smaller than the doped underlying layer, i.e. $\delta > 0$. There is additional voltage drop at the contact periphery and this leads to additional resistance. This additional resistance becomes extremely important for contacts with high sheet resistance and low specific contact resistivity and therefore complicate the CBKR measurements.[18]

2.4.2 Shockley Method

In this method, the potential difference between progressing pairs of contacts is plotted with respect to the pair distance. The function when extracted to zero potential gives the transfer length L_T , the distance over which most current transfers from one material to the other. The specific contact resistivity ρ_c can be calculated from Equation 2.21, where R_{SH} is the sheet resistance of the underlying layer.

$$L_T = \sqrt{\frac{\rho_c}{R_{sh}}} \quad (2.21)$$

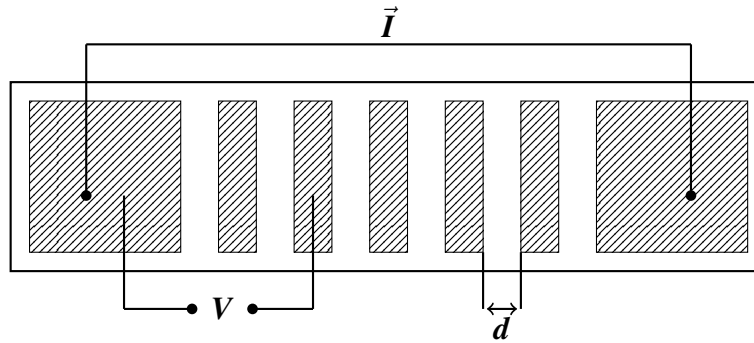


Figure 2.8: Ladder-structure contacts on doped-semiconductor region, top-down view.

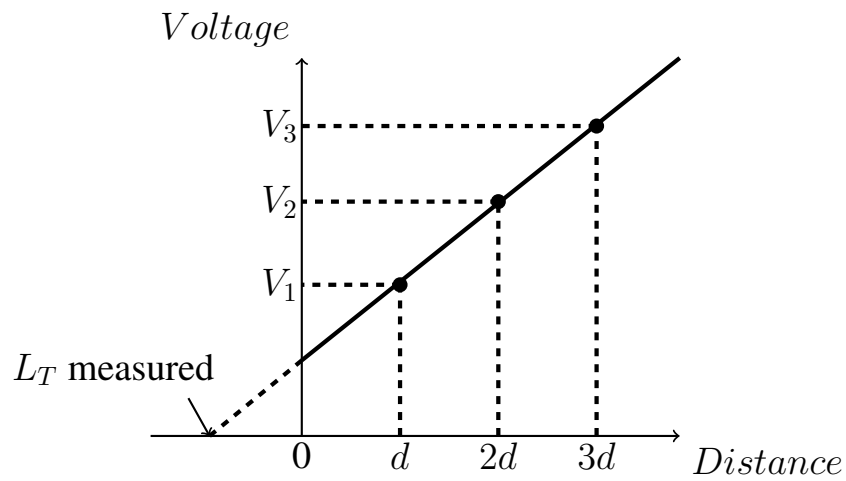


Figure 2.9: Extraction of the transfer length using the Shockley method

Detailed description of L_T is described in Chapter 4 that discusses the TLM Method in detail. Before diving into that topic, the technology behind the formation of these metal-semiconductor contacts needs to be properly understood. The next chapter on the Metal-Semiconductor contact technology serves this purpose.

Chapter 3

Metal-Semiconductor Contact Technology

Metal-semiconductor contacts need to have most, if not all of the following characteristics in order to be effectively utilized in Si technology. They need to have low contact resistance to n+ and p+ regions. They should be easy to form and have good compatibility with Si processing such as deposition, etching, cleaning etc. There must be no reaction or diffusion of the contact metal into Si, SiO₂ or any other materials used in back-end technology. There must also be no impact of the metal on the electrical characteristics of the shallow junctions. The contacts must also be thermally stable and reliable.

3.1 Aluminum Contact Technology

Aluminum has traditionally been favored to make metal-semiconductor contacts due to its good conductivity and the formation of a protective oxide on the top surface. It also fulfills most of the requirements of a good metal-semiconductor contact listed above. Usually, a 1-2 μ m thick layer of Aluminum is deposited on patterned Si wafer where it makes direct contact to the Si in the contact openings. It is then heated to ensure an intimate contact between the Al and the Si.

The use of aluminum to form contacts was predominantly used in the era of larger device sizes. As contact geometries began to shrink, an increase in the contact resistance

was observed in silicon-aluminum contacts. The processing temperatures for back-end silicon processing often reach 450-500°C. In an Al/Si system, the solubility of Si in Al is about 0.5-1% at those temperatures as shown in the phase diagram in Figure 3.1.

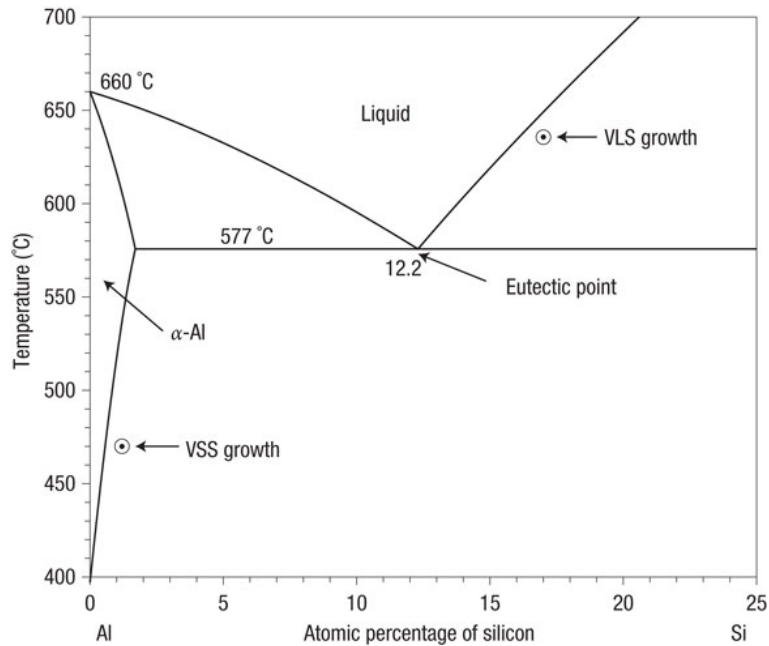


Figure 3.1: Al/Si phase diagram [21].

The Si atoms can diffuse into the Al due to their high diffusivity (about $100\mu\text{m}$ at 450° in 30 mins). This leads to the issue of junction spiking, where the Al is seemed to "spike" into the silicon junction leading to the formation of pits. These pits can be observed in Si after etching away the Al as seen in Figure 3.2. In modern contact dimensions, the spikes can be deep enough to destroy device operation. The spiking effect can be reduced by using Rapid Thermal Anneal (RTA) or Processing(RTP). The rapid increase in temperature would reduce the Si diffusion into Al. Another strategy is to add about 1-2% Si in the Al for the deposition in order satisfy the solubility requirement and prevent Al spiking during thermal processing.

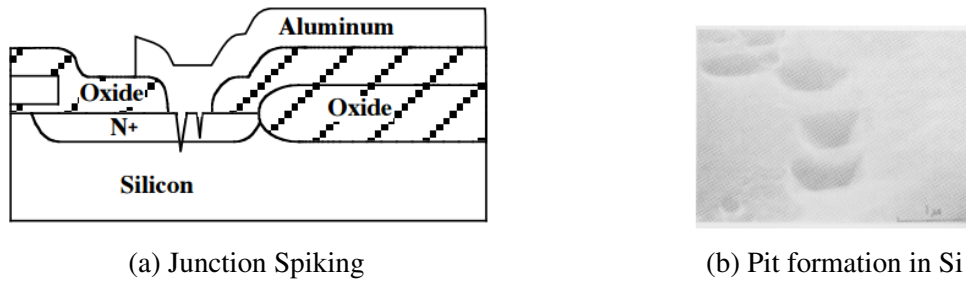


Figure 3.2: Pit formation and junction spiking [13].

3.2 Metal-Silicide Contact Technology

Silicides have been used for interconnects and contacts for many novel devices in the nanoelectronics and photonics industries in the modern era. Near noble and refractory metal silicides are used in the modern semiconductor devices due to their low resistivity and good adhesion to Si. They also provide low contact resistance to Si by forming ohmic contacts to n^+ or p^+ silicon. Apart from these critical benefits, silicides also have good thermal stability, high corrosion and oxidation resistance, low interface stress and high electromigration resistance. Silicides also have the inherent advantage of compatibility with other processes such as lithography and etching, thereby offering ease of integration into the semiconductor manufacturing process. Table 3.1 outlines some of the main properties of common metal silicides.

Property	TiSi ₂	CoSi ₂	NiSi
Formation Temperature °C	600-700	600-700	400-600
Thin Film Resistivity ($\mu\Omega cm$)	13-20	14-20	14-20
Schottky Barrier Height (n-Si, eV)	0.6	0.64	0.67
Si consumption ratio	2.27	3.64	1.83
Silicide thickness ratio	2.51	3.52	2.34

Table 3.1: Main properties of common silicides [3].

3.2.1 Formation of Silicides

The usual formation of metal silicides involves the following steps.

- Cleaning the wafer with a dilute HF and deionized water solution, followed by blowing dry using nitrogen gun or "spin-rinse-dry". This step gets rid of any native interfacial SiO₂ layer prior to metal deposition as metal needs to penetrate thin oxide layer in order to react with silicon to form the silicide.
- Metal is then deposited on the wafer using sputter deposition or epitaxial process.
- Wafer is then heat treated using furnace annealing or Rapid Thermal Processing (RTP) to form silicide at the metal-silicon interface.
- Removal of the unreacted metal using Piranha etch chemistry.

Formation of metal silicides are governed predominantly by growth kinetics over growth energetics. Only selective phases of the silicide are detected after thermal annealing of the metal films on silicon. The formation of multiphases in refractory metal/Si systems can however be observed through deeper and more refined analysis using better techniques such as high-resolution transmission electron microscopy (HRTEM) with fast Fourier transform (FFT) analysis.

Various different crystalline phases can be formed in a metal/Si system. For example, the Ti/Si systems forms as many as four different crystalline phases (Ti₅Si₃, TiSi, C49-TiSi₂ and C54-TiSi₂). Figure 3.3 shows a sample of the multiphases in Ti/Si. The identification of the initial phases of reaction for these silicides is difficult due to the close proximity and overlap of diffraction rings from their diffraction patterns.

The growth and formation of metal silicides are diffusion controlled or interface-reaction controlled and they can be formed far below the eutectic temperature, the temperature at which a particular mixture freezes or melts. The sequence of phase formation, dependence

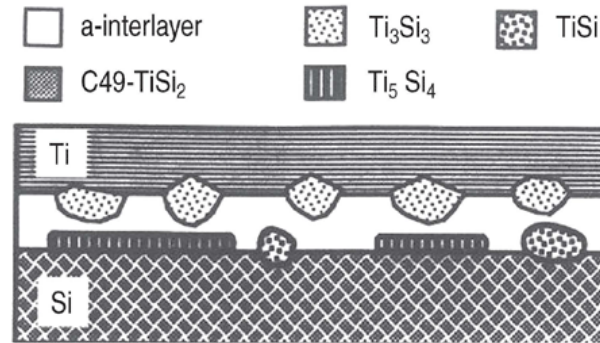


Figure 3.3: Multiphases in Ti/Si sample [3].

of phase growth and morphology of phase and interface structure can be demonstrated using cross-section transmission electron microscopy (XTEM). Inert markers such as ion implanted inert gases, metal deposited inert metal islands, or monitoring movement of neutron bombarded Si (radioactive Si) can be used to determine the dominant diffusion species in the silicidation reaction. The formation of metal-rich silicide, monosilicide and disilicide occurs at about 200, 400 and 600°C, respectively. At low temperatures like 200°C, not many Si atoms get released from its lattice. At temperatures like 600°C, lattice vibrations facilitate the release of Si atoms from the substrate.

3.2.2 Self-aligned Silicide (SALICIDE)

Self-aligned Silicide is used as a process to lower the resistance of the gate, source and drain areas in modern MOS transistors. It is beneficial as it forms low resistance contacts to source/drain regions without the need of an additional lithographic step. The metal is deposited all over the structure followed by a Rapid Thermal Anneal or Process (RTA or RTP) to form the metal silicide. Therefore, the process is Self-aligned. Ti, Co, Ni, Pd and Pt are can be used for the SALICIDE process but Ti, Ni and Co are most commonly used in the IC industry. Figure 3.4 shows self-aligned silicide in a MOSFET.

Usually, a two step process is used to form the SALICIDE. After the initial formation

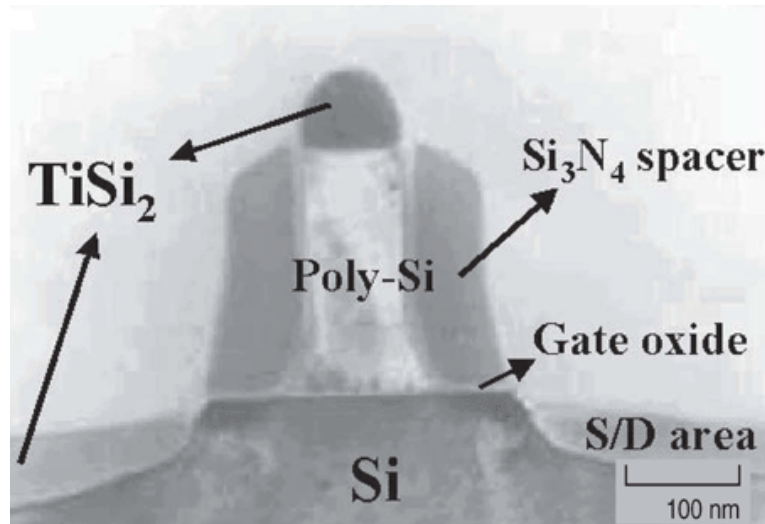


Figure 3.4: SALICIDE on MOSFET source/drain [3].

of the metal silicide mentioned above, the unreacted metal is etched away. Depending on the choice of metal and annealing conditions, a high or low-resistivity phase of the silicide is obtained. A second RTA step can be used to transform the silicide from a high-resistivity to a low resistivity phase.

TiSi₂ with a formation temperature of 800°C to 900°C was initially used as SALICIDE for the CMOS process. As linewidths continued to shrink, CoSi₂ showed increased promise but was limited to high series resistance of the silicided lines. NiSi has been the material of choice for sub-90nm technology nodes. Issues like NiSi pipes have been observed in industry beyond the 20nm node and it is possible that TiSi₂ may be reintroduced for nodes beyond 20nm.

TiSi₂ Technology

Due to its low resistivity, thermal stability and compatibility with the Si process, titanium silicide was one of the first few silicides to be considered for Si-based devices.

Formation Titanium disilicide is of greatest interest to the Si nanoelectronics amongst the several forms, crystal structures and material properties of titanium silicides that can be

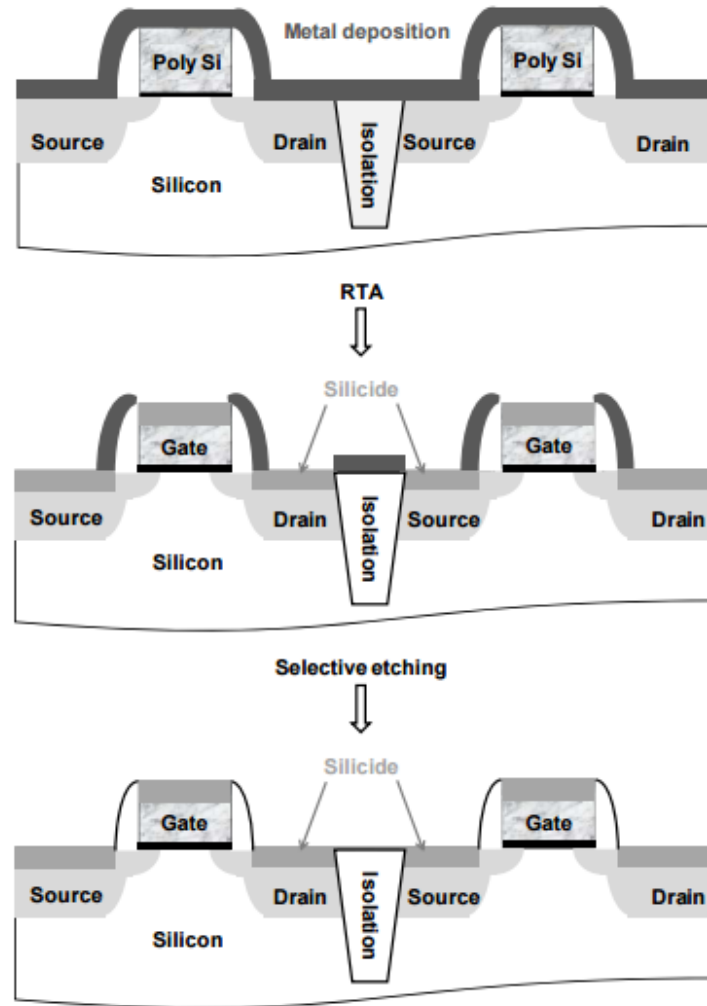
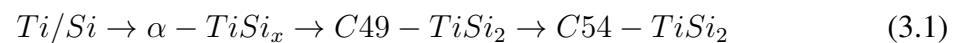


Figure 3.5: Description of SALICIDE process[17].

formed. It offers the lowest resistivity and good thermal stability during post-processing. The SALICIDE process used for $TiSi_2$ formation is shown in Figure 3.5. The phase formation sequence for the silicidation reaction of Ti/Si involves the following reaction path.



Not all the phases appear during heat treatment. The C54 phase offers very low resistivity at equilibrium depending upon method of fabrication. The equilibrium Ti-Si binary

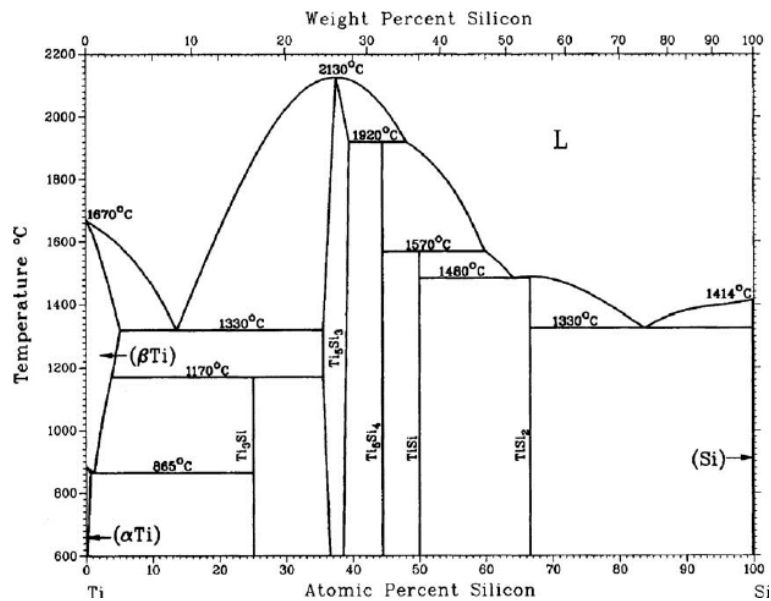


Figure 3.6: Ti-Si equilibrium binary phase diagram [12].

phase diagram is shown in Figure 3.6.

The *in situ* resistance versus temperature curve for Ti/poly-Si bilayer deposited over silicon dioxide during furnace annealing at 10°C/min shown in Figure 3.7 has four distinct stages in resistance.

1. Linear increase in the resistance with increasing temperature from 25 °C to 350°C.
2. Steep increase in resistance following region 1.
3. Sharp decrease in resistance \sim 550°C.
4. Another sharp drop at \sim 700°C

Integration and Scaling Successful integration of TiSi₂ requires adequate consideration and understanding of the effects of dopant type on phase formation and dopant redistribution during silicidation. The effect of impurities, formation ambients, reactions to oxide and/or nitride spacers needs to be understood. The presence of n or p-type dopants in the order of 10²⁰ /cm³ retards the phase formation and reaction kinetics. Dopant diffusion and

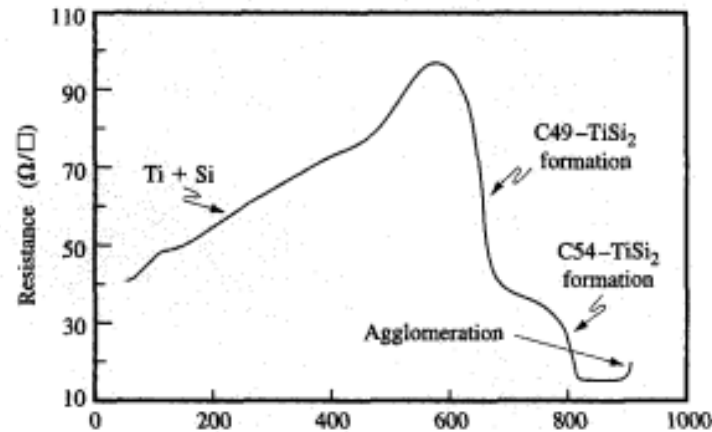


Figure 3.7: Resistance versus temperature curve for *in situ* annealing of Ti/poly-Si [11].

redistribution in grain boundaries of titanium silicide is a concern as it affects source/drain and contact resistance. Dopant segregation can also be electrically active providing additional charge carriers at the interface thereby reducing the silicide/Si interfacial resistance [3]. The reaction between the Ti and oxide or nitride spacers due to silicidation needs to be minimized as residues formed in the reaction can lead to gate-to-source/drain leakage or shorts. These shorts can also occur due to lateral encroachment of the silicide into the gate-to-source/drain regions.

Titanium silicide scaling has conventionally been achieved by reducing the Ti film thickness but this leads to issues such as incomplete C49-to-C54 phase transformation and enhanced agglomeration. The minimum temperature to transform the silicide shifts upward and the maximum temperature before the onset of agglomeration shifts downward leading to a shortening of the silicidation process window for shrinking device dimensions. Increased silicide thickness offers lower sheet resistivities and better defect margin but increases the Si consumption that increases the risk of device leakage and is incompatible with ultra-shallow junction formation. Figure 3.8 below sums up the operable SALICIDE process window for reduced Ti thickness.

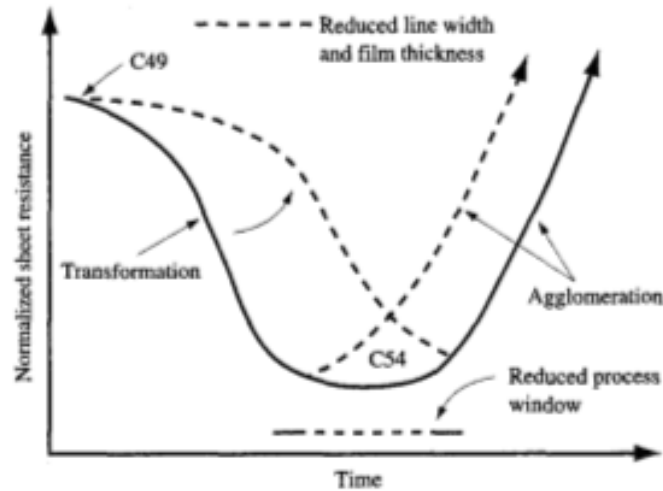


Figure 3.8: SALICIDE process window for reduced linewidth and film thickness [11].

NiSi Technology

Nickel silicides have more recently been investigated for use in microelectronic applications due to their formation in thinner films, low thermal budget of formation, low resistivity in narrow dimensions and low device leakage.

Formation The Ni/Si phase formation sequence is far more complicated than TiSi_2 and one can expect up to 11 phases, 6 of which are stable at room temperature. The phase formation sequence becomes far more complicated and there is possible dependence on processing parameters and substrate variations such as dopant type and concentration and cleaning conditions.

The thermal budget of the formation of the low resistivity NiSi phase is much lower than its counterparts and is therefore much easier to form as a monosilicide. The lower temperature of formation of NiSi is due to its higher concentration and diffusivity.

The process of formation of NiSi is predominantly diffusion controlled. This is contrary to nucleation controlled reactions for low resistivity Ti and Co silicides where the reaction is rapid, non-uniform and has some characteristic surface roughness. A diffusion controlled

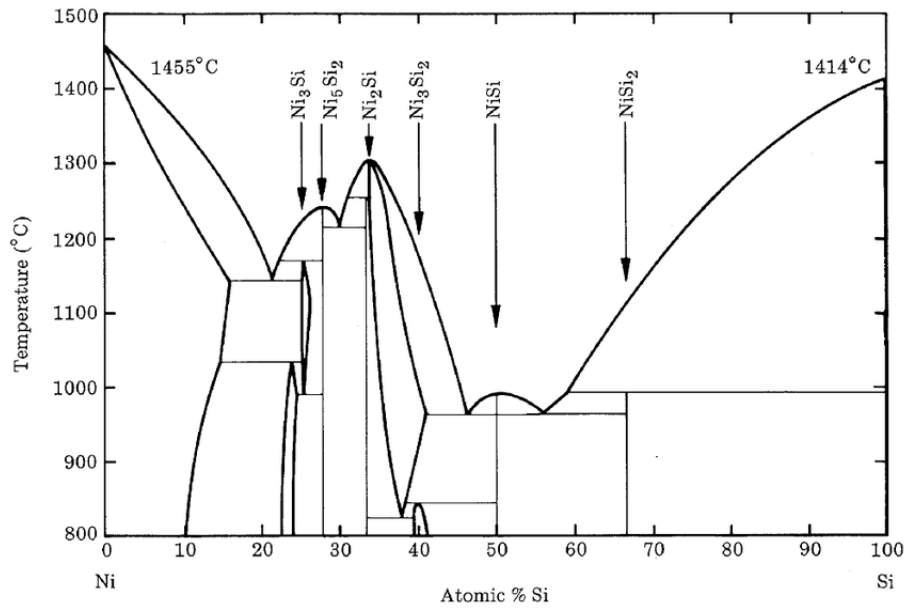


Figure 3.9: Ni/Si phase diagram [19].

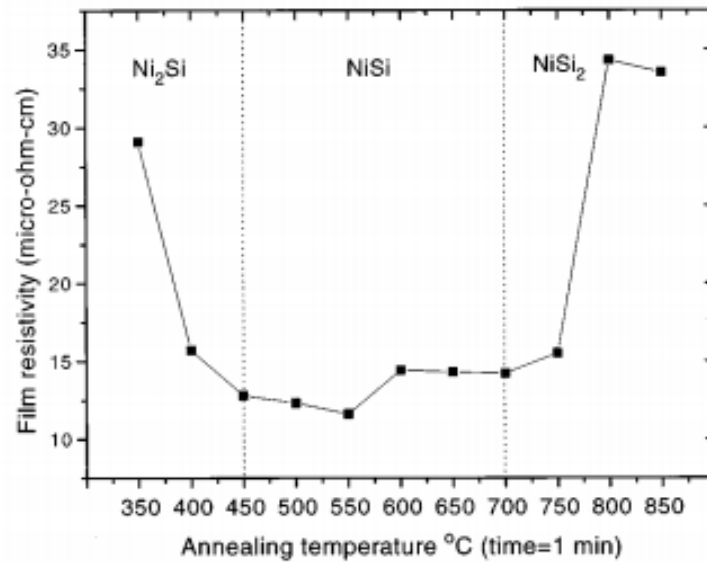


Figure 3.10: Film resistivity versus annealing temperature for NiSi [4].

reaction involves planar growth fronts of new phases following the standard reaction [3].

Integration and Scaling Apart from the inherent advantages of NiSi over its competitive silicides, there are still some challenges associated with its integration into the conventional

semiconductor manufacturing. Undesired agglomeration of NiSi and formation of NiSi₂ at low temperatures, excessive Ni diffusion on narrow Si or poly-Si lines can lead to abnormally high junction leakages. The performance and yield of NiSi on narrow poly-Si gate is far superior than similar silicides. Gate patterning does not limit silicide formation for NiSi as no degradation in resistance is observed which is usually linked to agglomeration, stress and voiding effects.

Due to the presence of more grain boundaries on NiSi films on poly-Si substrates, there is faster diffusion of Ni during phase formation. This process can be optimized to give thicker silicide on poly-si areas and less silicide on active junctions. This would be advantageous for device applications based on Silicon-On-Insulator (SOI) substrates as source and drain regions of the devices would require very small amounts of Si consumption. The formation of high resistivity NiSi₂ can also limit the NiSi process. Local stresses can lead to the formation on NiSi₂ even if it does not normally occur in temperatures below 800°C. NiSi provides comparatively higher contact resistance to heavily doped p-type substrates over heavily doped n-type, but still lower than contacts with CoSi₂.

Chapter 4

Transmission Line Measurement (TLM)

Method

The Transmission Line Measurement or TLM method is popularly used to determine the specific contact resistivity of metal-semiconductor interface in the modern semiconductor industry. Originally proposed by Shockley, it involves current voltage measurements on adjacent contacts with variable spacing between them. It utilizes a similar ladder structure as observed in the Shockley method but the current is not perturbed by contacts in between for this method. The total resistance R_T between any two contacts (of length L and width W) separated by a distance d could be measured and plotted as a function of d . The resulting equation between R_T and R provides an estimate of ρ_c through the so called transfer length L_T , measured from the intersection of the R curve for $R_T = 0$.

4.1 Transmission Line Measurement (TLM) Structure

The Transmission Line Measurement (TLM) structure involves contacts fabricated on diffused semiconductor regions of a particular sheet resistance R_{SH} depending upon the application. These diffused regions are isolated from their surroundings by using trench or MESA isolation. If MESA isolation is used, the depth of the MESA should be greater than

the junction depth (x_j) of the diffused carriers in order to avoid current leakage. The metal contacts are fabricated with a length L and width W and incrementing spacings between each adjacent contact d_1, d_2, d_3 and d_4 . Figure 4.1 shows a top-down view of a fabricated TLM structure.

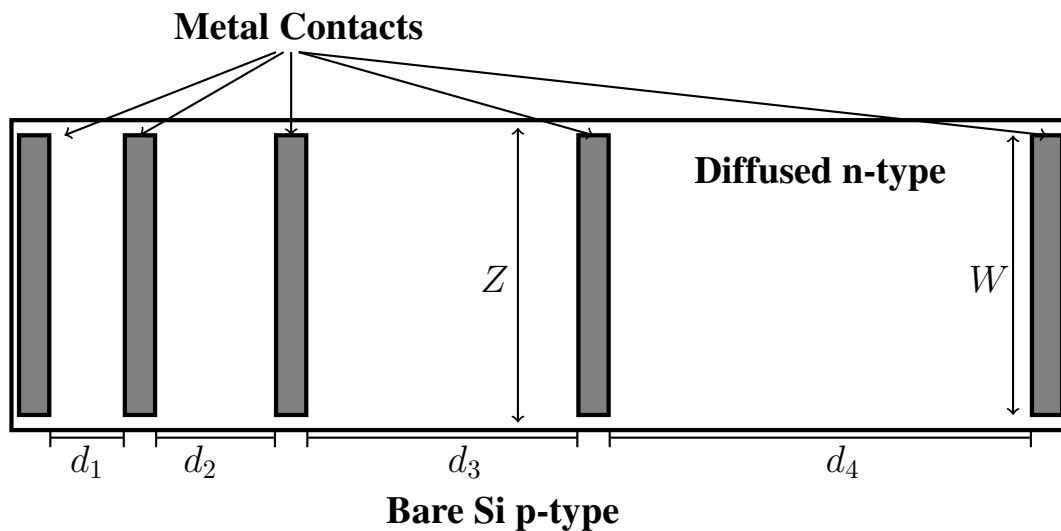


Figure 4.1: Top-down view of TLM structure.

Insulating oxide can be used to separate the contacts. The contacts can be wired to bond pads with thick wires for ease of measurement with small geometries. The horizontal view of a basic TLM structure can be observed in Figure 4.2 below.

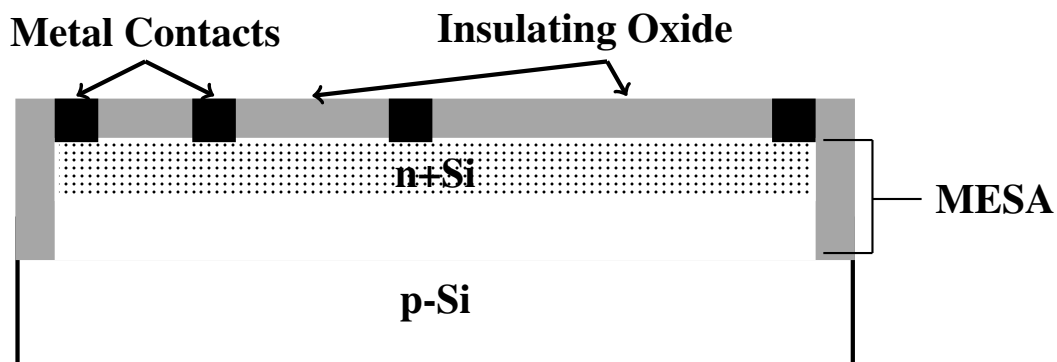


Figure 4.2: Horizontal view of TLM device structure.

4.2 ρ_c Extraction

I-V measurement is carried out on each adjacent contact and the resistance is obtained from the slope of the curve. The resistance is then plotted as a function of the contact spacing d . (Figure 4.3)

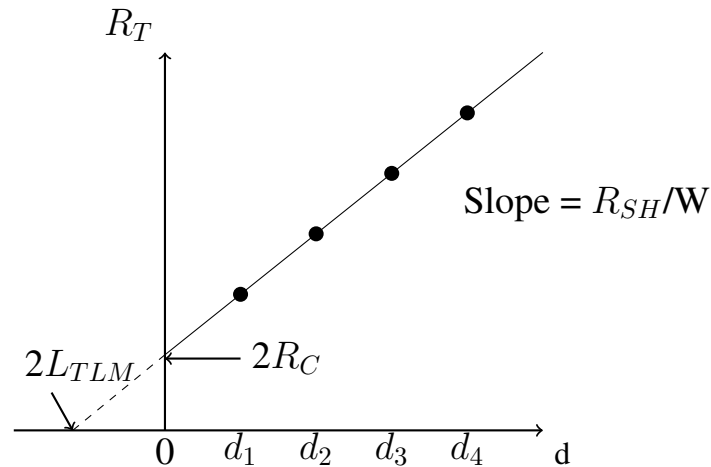


Figure 4.3: Plot to extract transfer length from the TLM method.

The specific contact resistivity is usually obtained from the plot using the extracted transfer length L_T and sheet resistance R_{SH} . An equation for the total resistance (R_T) of the TLM structures can be extracted from the above plot.

$$R_T = 2R_C + \left(\frac{R_{SH}}{W}\right)d \quad (4.1)$$

Upon consideration of the path of the current under a contact, it can be observed that the width of the current path under the contact or the distribution of the current density is directly dependent of the level of specific contact resistivity ρ_c .

Figure 4.4 describes the flow of current under a metal contact within the semiconductor region. For very small values of ρ_c the current flows quickly into the contact and only the edge of the contact area is used in conduction(Figure 4.5(a)). For high values of ρ_c , the

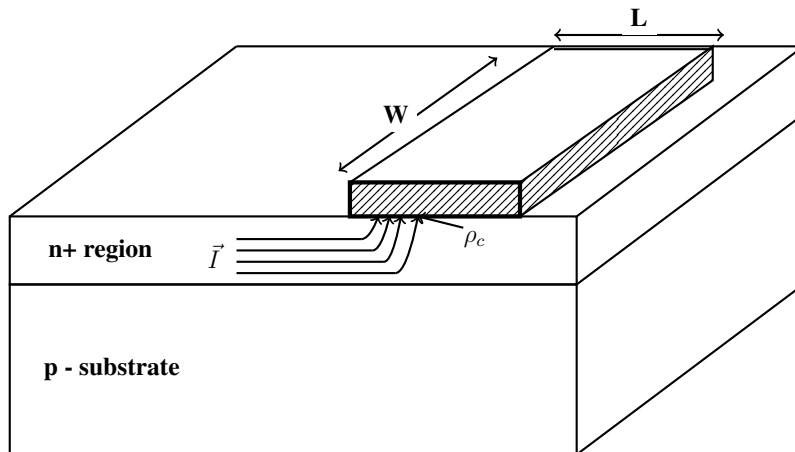


Figure 4.4: Current path under metal contact to n-type semiconductor.

current path is expanded due to high transition resistance and a larger amount of the contact is used for conduction (Figure 4.5(b)).

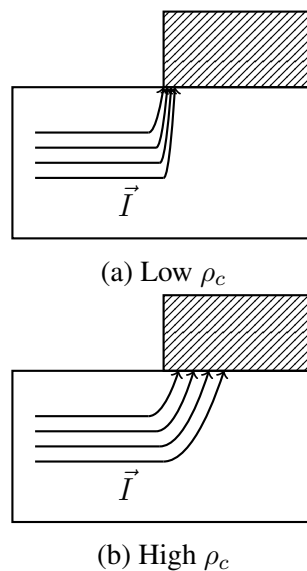


Figure 4.5: Current flow into the contact for low and high ρ_c .

The characteristic length when the voltage drops to $1/e$ of its value is called the transfer length L_T . The length of the contact must be chosen in close consideration of the transfer length. The transfer length extracted from the TLM method is the half the value of the x-axis intercept of the total resistance versus pad spacing plot. This transfer length is depicted

as L_{TLM} .

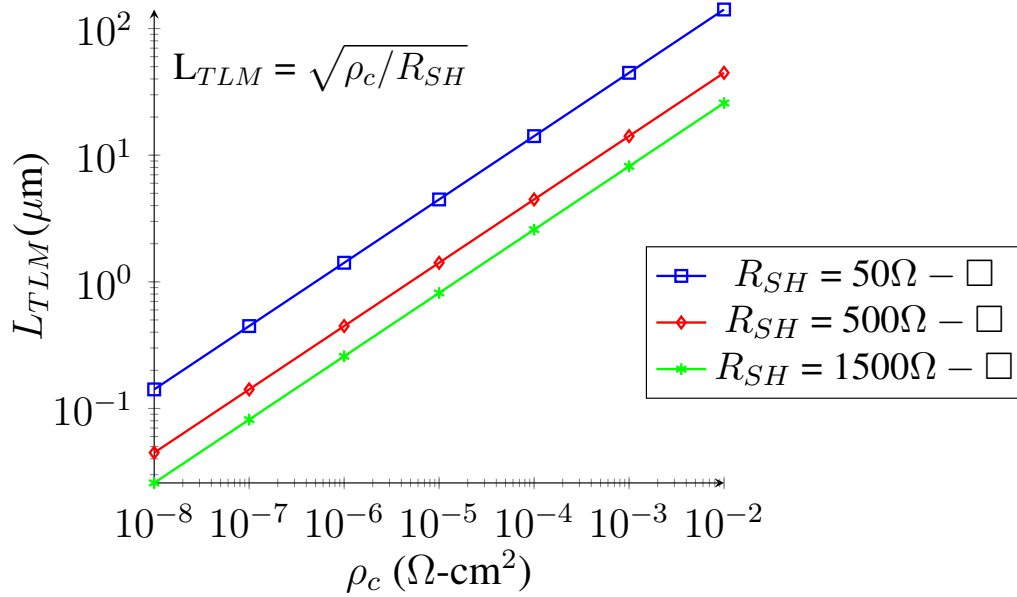


Figure 4.6: Transfer length as a function of ρ_c .

The transfer length as a function of the specific contact resistivity ρ_c is plotted in Figure 4.6 above. It can be observed that for a particular application of a given sheet resistance R_{SH} and anticipated ρ_c , the transfer length can be estimated and the length of the contact must be design with consideration of the transfer length. Smaller contact lengths can lead to current crowding and larger contact lengths are a waste of usable device area.

The effect of metal resistivity can be included in ρ_c extraction by the means of the following equation below.

$$R_c = \frac{L'_T}{Z} \left[\frac{(\rho_m^2 + R_{SH}^2)}{(\rho_m + R_{SH})} \coth(L/L'_T) + \frac{\rho_m R_{SH}}{\rho_m + R_{SH}} \left[\frac{2}{\sin(L/L'_T)} + \frac{L}{L'_T} \right] \right] \quad (4.2)$$

where $L'_T = \sqrt{\frac{\rho_c}{\rho_m + R_{SH}}}$

ρ_m is the resistivity of the metal. For aluminum ρ_m is $2.5 \times 10^{-8} \Omega\text{-m}$ and is neglected

in calculations in this work due to its small difference percentage wise.

Chapter 5

Contact Resistance Modeling

Accurate modeling of the contact resistance is essential in understanding metal-semiconductor contacts as it is practically difficult to fabricate contacts that have a uniform current density over its conduction area. It is usually considered the limit as the area goes to zero. In real devices, the current distribution is non-uniform and therefore the definition of ρ_c which involves a uniform current density for contact resistance per unit area becomes a bit ambiguous.

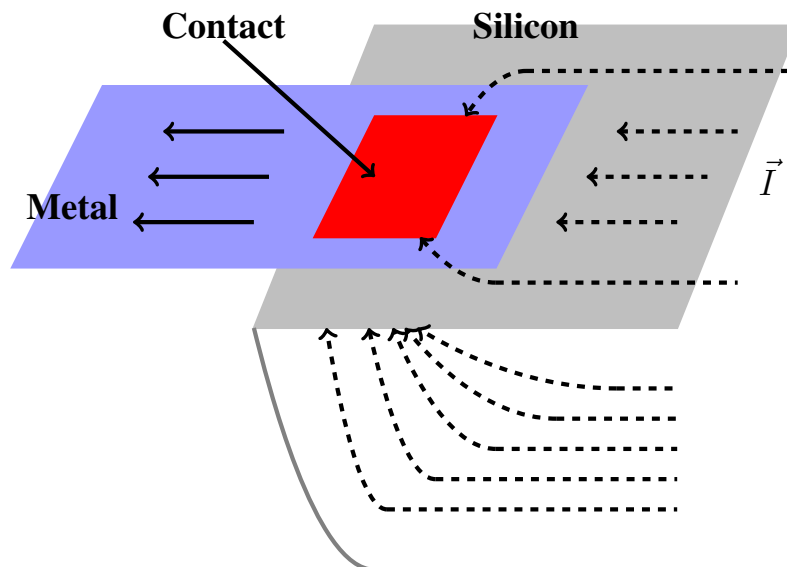


Figure 5.1: Non-uniform current distribution in a contact.

The contact system is described by transport equations. Poissons and two-carrier continuity equations in 3-D can be adequately used to describe the model. These equations are more often than not, simplified into 2-D or 1-D equations.

5.1 Three-Dimensional Model

In the three-dimensional model, the topology of the contact can vary in three spatial dimensions of x,y and z. Both, the metal potential (U_m) and semiconductor potential (U) are functions of the spatial coordinates. The majority carrier equation outside the contact is given by

$$\nabla \cdot J = \frac{\delta J_x}{\delta x} + \frac{\delta J_y}{\delta y} + \frac{\delta J_z}{\delta z} = 0 \quad (5.1)$$

The current density in the semiconductor is given by J , where U is the potential at a coordinate (x,y,z).

$$\vec{J} = -\sigma \vec{E} = \sigma \nabla U \quad (5.2)$$

By combining Equations (5.1) and (5.2), we get

$$\nabla \cdot \sigma \nabla U = 0 \quad (5.3)$$

Similar expressions can be applied to the metal region. Usually, the metal conductivity is much larger than that of the semiconductor. Therefore, the metal potential U_m becomes constant over the entire interface. The only variable that remains is the semiconductor potential U and it governs the entire metal-semiconductor system. The total current evaluated over a surface of area A is given by Equation 5.4. Solving the system of equations with appropriate boundary conditions can give us the necessary information regarding the metal-semiconductor contact resistivity.

$$I_{tot} = - \int \vec{J} \cdot dA \quad (5.4)$$

Several approximations can be made for heavily doped semiconductor junctions. First, the effect of minority carriers is neglected. This is equivalent to neglecting the depletion layer depth or band bending at the contact interface. The total current density is approximately the same as the majority carrier density because the metal-semiconductor interface injects far more majority carriers than minority carriers. Second, due to this majority carrier domination, the majority carrier concentration is approximated to the active dopant density. Hence, only majority carrier continuity equations are used to solve for the semiconductor region beneath the contact. The three-dimensional model can get very difficult in computation and generalization. Therefore, two-dimensional models can be developed while still providing useful insights.

5.2 Two-Dimensional Model

In the two-dimensional model, the contact interface is considered as a 2-D surface perpendicular to the z -axis. The diffused layer is located beneath the metal-semiconductor interface with an effective thickness that is assumed to be the junction depth. This model lumps the effects of the z -axis into a single parameter, R_{SH} , the sheet resistance of the diffused layer.

$$R_{SH} = \left(\int \sigma(z) dz \right)^{-1} \quad (5.5)$$

Since the metal layer is usually more conductive than the semiconductor layer, the metal potential U_m is assumed to be constant. If the metal potential is set to zero, the 3-D equations can be simplified into the following equation called the Helmholtz.

$$\nabla^2 V = \frac{R_{SH}V}{\rho_c} = \frac{V}{L_T^2} \quad (5.6)$$

In the bulk region with no contact surface, the potential can be described by Laplace's equation

$$\nabla^2 V = 0 \quad (5.7)$$

The above equations can be solved to obtain the I-V characteristics and extract values of ρ_c .

5.3 One-Dimensional Model

The one-dimensional or 1-D model is a further simplified model where the variation in the y-axis is neglected. Since the potential changes only slightly in other axes, the Helmholtz equation then becomes.

$$\frac{\nabla^2 V}{\delta^2 x} = \frac{V(x)}{L_T^2} \quad (5.8)$$

Upon application of the boundary conditions, the Laplace's equation can be reduced to Ohms law and the potential can be shown as

$$V(x) = V_i \frac{\cosh\left(\frac{L-x}{L_T}\right)}{\cosh\left(\frac{L}{L_T}\right)} \quad (5.9)$$

The current is given as

$$I_{tot} = \frac{W}{R_{SH}} \frac{\delta W}{\delta x} \Big|_{x=0} \quad (5.10)$$

The above equations can be used to extract the contact resistance. The 1-D model can be further reduced to provide an even more intuitive feel to the contact resistance extraction. This is given by the Zero-Dimensional model.

5.4 Zero-Dimensional Model

The 1-D model can be simplified to a 0-D model in the cases of large contact windows, very high values of ρ_c or very small contacts. This model assumes that the current density entering the contact window is uniform and the potential is constant in the semiconductor layer. ρ_c is considered as a macroscopic quantity and is given by

$$R_c = \frac{\rho_c}{A} \quad (5.11)$$

5.5 Lumped Circuit Model

According to the lumped circuit or distributed resistive network model, the behavior of the current flow under a contact can be explained using a resistance network. A distributed resistive network can be simulated in order to understand the metal-semiconductor contact resistance.

The voltage distribution under the contact works out as

$$U(x) = U_0 \exp \left[- \left(\frac{x}{\sqrt{\rho_c / R_{sh}}} \right) \right] \quad (5.12)$$

When the voltage distribution is plotted with respect to the distance across which the

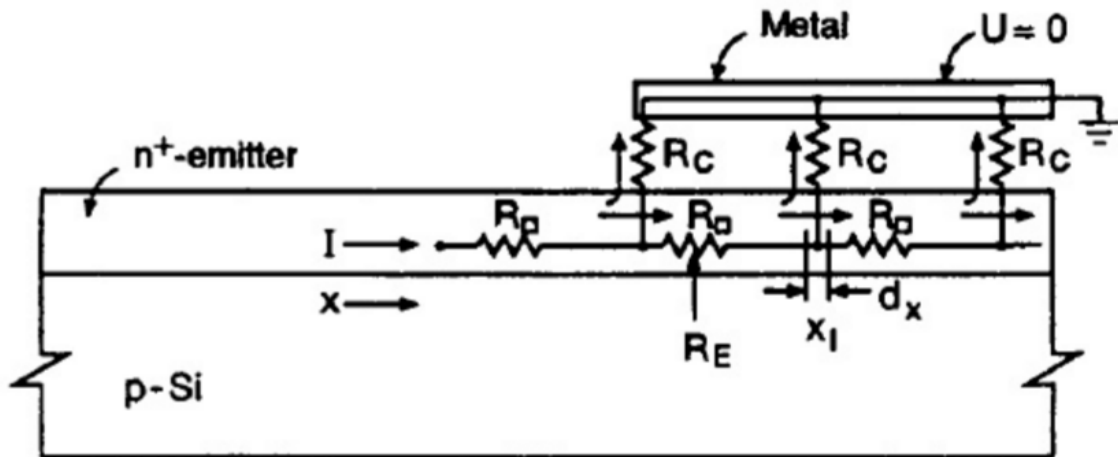


Figure 5.2: Resistive network for metal-semiconductor contact resistance [8].

current flows, the exponential dependence can be noted.

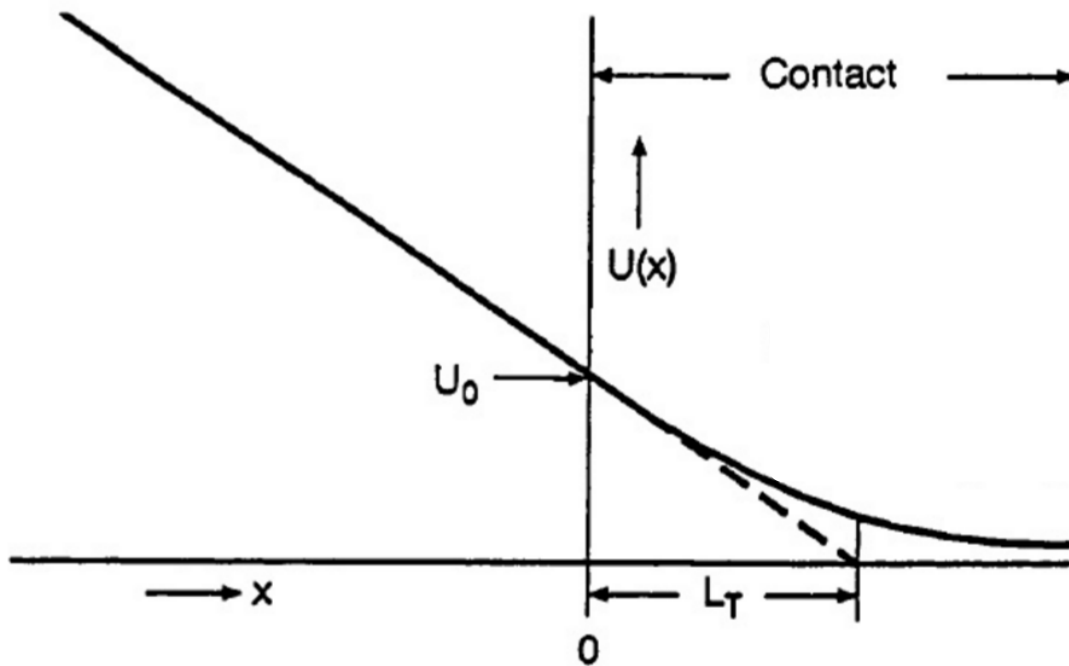


Figure 5.3: Voltage distribution under contact [8].

It can be observed from Figure 3.3, the voltage drops to $1/e$ of its value after a characteristic length L_T . This is called the transfer length and is a characteristic variable for the current path. It can be expressed as function of the specific contact resistivity (ρ_c) and the sheet resistance R_{SH} through the following equation.

$$L_T = \sqrt{\frac{\rho_c}{R_{SH}}} \quad (5.13)$$

Mathematical analysis of the above expressions leads to the following value for the specific contact resistance.

$$\rho_c = \left(\frac{R_c W}{\coth\left(\frac{L}{L_T}\right)} \right)^2 * \frac{1}{R_{sh}} \quad (5.14)$$

Due to the \coth dependence, two limiting cases can be observed on the relation between L and L_T .

- For $L < 0.5L_T \rightarrow \coth\left(\frac{L}{L_T}\right) \approx \frac{L_T}{L} \Rightarrow \rho_c = R_c W L$
 - This is known as the **Short Contact Approximation**
 - Here, ρ_c is dependent on the length of the contact.
- For $L > 1.5L_T \rightarrow \coth\left(\frac{L}{L_T}\right) \approx 1 \Rightarrow \rho_c = R_c W L_T$
 - This is known as the **Long Contact Approximation**
 - Here, ρ_c is only dependent on the fraction of the contact used in current conduction i.e. L_T .

The two different approximations can be better understood by looking at the graph of the $\coth(x)$ function in Figure 5.4. For very small values of $x = L/L_T$, the function approximates to x or L/L_T . For very large values of x , the function retains a constant value of 1.

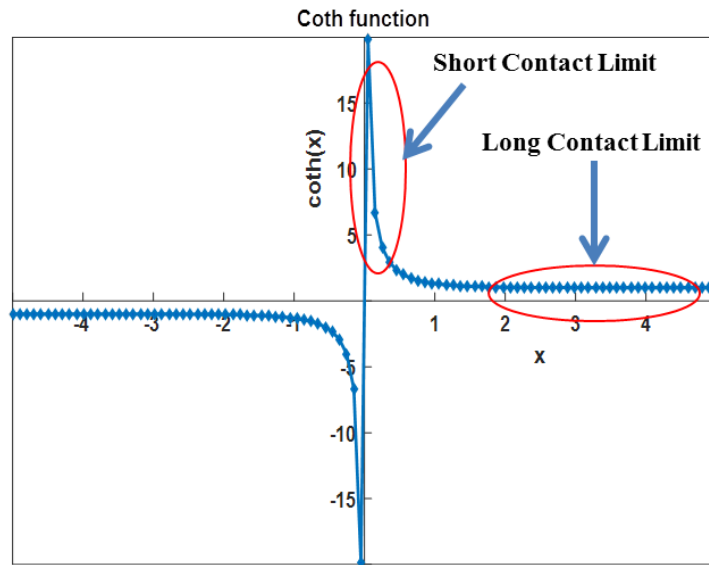


Figure 5.4: Coth function

The long contact approximation of this model has been widely used as legacy for ρ_c extraction and can potentially be the cause of incorrect values if appropriate contact geometries are not used. An example of this was observed in a paper published by BrightSpot Automation, LLC [6]. Although the length of the contact was $65 \mu\text{m}$, the measured transfer length was significantly larger than it in various cases. It was pointed out that the use of the approximated TLM formula was not applicable for the contact dimensions used in the study and the use of the generic TLM formula with no approximations gave better results. A summary of the recalculations are shown in Table 5.1.

Due to the recalculations carried out, the need for better understanding of the generic formula that has TLM length dependence was highlighted.

The lumped distributed circuit network model for the TLM measurement is limited in certain ways. In this model, the width of the TLM contact (W) is considered to be infinitely large when compared to other dimensions and its effect on the ρ_c extraction is neglected. The model also does not take into account the current crowding at the edge

L_T	$L_T < L$	L_T Recalc.	$\rho_c(\text{m}\Omega\text{-cm}^2)$	ρ_c Recalc.($\text{m}\Omega\text{-cm}^2$)
14.4 μm	$L_T < L$	21.67 μm	0.18	0.18
33.3 μm	$L_T < L$	9.87 μm	0.93	0.86
17 μm	$L_T < L$	18.69 μm	0.26	0.26
23.3 μm	$L_T < L$	13.79 μm	0.45	0.44
80.5 μm	$L_T > L$	5.88 μm	5.24	2.34
25.5 μm	$L_T < L$	12.66 μm	0.58	0.56
46.9 μm	$L_T < L$	7.63 μm	1.86	1.45
65.8 μm	$L_T > L$	6.34 μm	3.63	2.08
17.6 μm	$L_T < L$	18.00 μm	0.27	0.27
55.8 μm	$L_T < L$	6.87 μm	2.61	1.77
109.9 μm	$L_T > L$	5.42 μm	10.05	2.83
26.4 μm	$L_T < L$	12.21 μm	0.6	0.58

Table 5.1: Recalculation of ρ_c from general formula.

of the contact and the constriction (spreading) resistance. It is also assumed that ρ_c and R_{SH} are considered uniform throughout the entire structure. The resistivity of the metal ρ_m is initially neglected and metal lines are therefore equipotential. For these reasons, exact field solution model can potentially provide detailed insight into contact resistance and current crowding. It is discussed in the following section.

5.6 Exact Field Solution Model

The exact field solution model is the one of the most recent models for contact resistance extraction. This model involves the consideration of bulk regions I and II with dimensions of h_1 , h_2 , a and b . The resistivity of these regions are ρ_1 and ρ_2 . This model utilizes fourier series analysis methods to solve the boundary conditions at the different regions and therefore is also called the Fourier Series Analysis model.

A voltage V_0 is given at terminal EF and ground is applied to terminal BC. An interfacial layer of specific contact resistivity ρ_c is sandwiched between layer I and II. All other boundaries of the contact are electrically insulated. Boundary conditions across this

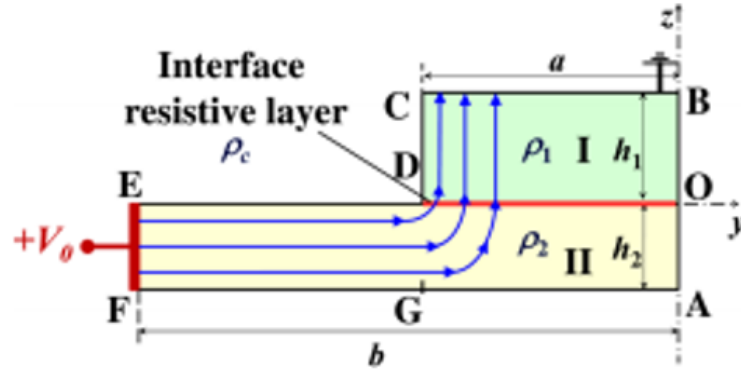


Figure 5.5: Electrical contact assumed for Finite Element Model [24].

infinitely thin interfacial layer are given by the normal components of the current density across the interface, J_z , and the potentials Φ_I and Φ_{II} in regions I and II respectively.

$$J_z = -\left(\frac{1}{\rho_1}\right) \frac{\delta\Phi_I}{\delta z} = -\left(\frac{1}{\rho_{II}}\right) \frac{\delta\Phi_{II}}{\delta z}; \rho_c J_z = \phi_{II}(y, z = 0^-) - \Phi_I(y, z = 0^+) \quad (5.15)$$

Fourier series expansion methods are used to solve for Φ_I and Φ_{II} for values of $h_1, h_2, a, b (> a)$ and including the interface resistance ρ_c . The total resistance from EF to BC can be given by the following equation.

$$R_T = \frac{\rho_2(b-a)}{h_2 W} + \frac{\rho_2}{2\pi W} R_{c,Total} \quad (5.16)$$

The first term represents the thin film resistance from EF to DG and the second term represents the total contact resistance in its normalized form as $R_{c,Total}$. W is the width of the contact in the dimension perpendicular to the paper. This model is applicable for the limit $\rho_c \rightarrow 0$. It takes into account the fringing field near the contact edge and effects of current crowding and constriction (spreading) resistance. It also includes the effect of the electrode properties ρ_1 and h_1 . The transfer length $L_{T,FT}$ in this case is defined as

the length of the contact interface over which 63.21% of the current transfers from the conducting layer into the contact. This matches the definition used for the transfer length in conventional TLM, where $L_{TLM} = (\rho_c/R_{SH})^{1/2}$. The exact field solution model can be very helpful in understanding the nature of the flow of current into and beneath the contact. It can assist us in providing a systematic evaluation of the current crowding and spreading resistance in thin film contacts made with very large contrasts in dimensions and resistivities [25]. This model can be used to define a transfer length ($L_{T,FT}$) which can then be compared to the conventional TLM transfer length (L_T or L_{TLM}). The comparison between L_T and $L_{T,FT}$ can assist us in evaluating the validity of a certain model over the other. It can also help in picking an optimum value of the length of the contacts used in the TLM method for application specific dimensions and contact resistivities. The optimum values of the transfer length would be the range of values for resistivity and geometry for which both L_T and $L_{T,FT}$ agree.

The model considers a pair of contacts that are identical and formed on the top of a conducting layer on top of an insulating substrate.

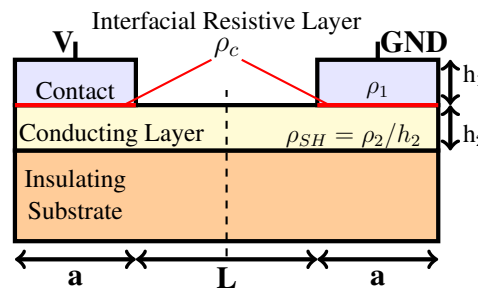


Figure 5.6: Two contact model for the Exact Field Solution Model.

A Fourier Series based analysis of the current density can be carried out of the above two-contact model in order to determine the transfer length or $L_{T,FT}$ for different cases such as changing ρ_c , a , h_1 , h_2 and ρ_1 .

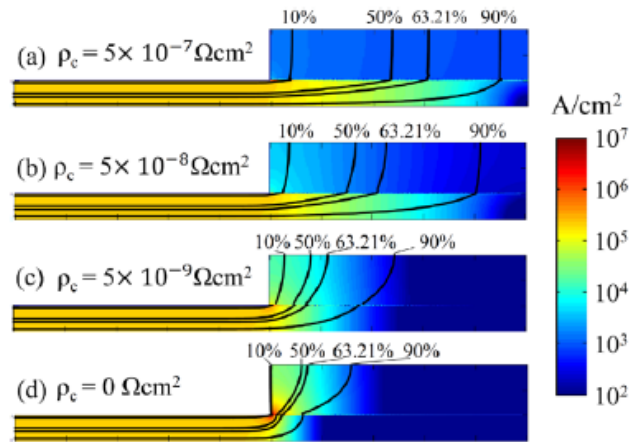
Initial simulations were carried out by Dr. Peng Zhang [25] in order to understand the

effect of varying the parameters in the model on the transfer length and are summarized in this section. The effect of varying interfacial contact resistivity (ρ_c), contact area (largely dependent upon a), thickness of conducting layer (h_2) and height of electrode (h_1) were carried out through the exact field solution model.

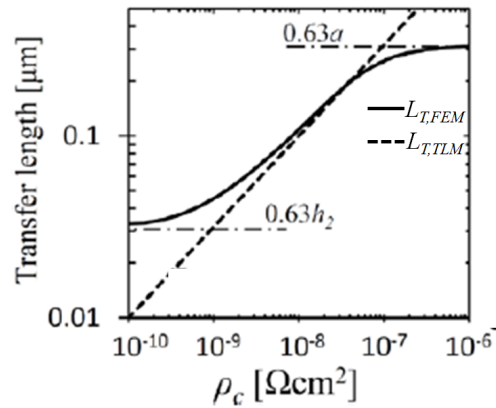
The effect of varying the contact resistivity of the interfacial layer or the specific contact resistivity (ρ_c) was modeled using exact field solution. Its effect on the transfer length was observed using current density distributions and plots of transfer length versus ρ_c . The current transfer length can be plotted as a function of the interfacial contact resistivity (ρ_c). This transfer length, called $L_{T,FT}$ can also be compared with the conventional transfer length from the TLM method L_{TLM} . Unless otherwise specified the simulations used $a=0.5\mu\text{m}$, $L/2 = 10\mu\text{m}$, $h_1 = 100\text{nm}$, $h_2 = 50\text{nm}$, $\rho_1 = 2.44 \times 10^{-8} \Omega\text{-m}$ and ρ_{SH} as $100 \Omega/\text{sq}$. The total current was kept fixed at $50 \mu\text{A} \mu\text{m}^{-1}$.

5.6.1 Changing Contact Resistivity of Interfacial Layer

From the above modeling, it can be observed that the current density at the edge of the contact increases significantly on decreasing the interfacial contact resistivity or the specific contact resistivity (ρ_c). There is increased current crowding at the edge of the contact for lower values of ρ_c . The transfer length $L_{T,FT}$ from this model can be extracted as the characteristic length to which 63.31% of the current flows. A comparison of $L_{T,FT}$ and $L_{T,TLM}$ can be carried out where $L_{T,TLM}$ is the conventional TLM transfer length. According to Figure 5.7(b), it can be observed that the upper limit of $L_{T,FT}$ is bound to 63.21% of the length of the contact and the lower limit is 63.21% of the height of the conducting layer. It can be generally observed that L_T increases as ρ_c increases. This is true irrespective of the measurement technique used. Further, it can be seen that the Exact Field solution model agrees with the conventional TLM model for a small range of values



(a)



(b)

Figure 5.7: (a) Current density distribution on changing ρ_c from the exact field solution model. (b) Transfer length as a function of interfacial contact resistivity (ρ_c) [25].

of ρ_c .

5.6.2 Changing Contact Length

The variation of the transfer length on changing the length of the contact a was also modeled and its results can be observed from Figure 5.8. The transfer length from the conventional TLM method $L_{T,TLM}$ has no change upon changing the length of the contact. $L_{T,FT}$

increases till about $2L_{T,TLM}$ but does not change much beyond this point. Therefore, according to the exact field solution model when the length of the contact is very small, the current flows very rapidly into the contact leading to small values of transfer length. Hence, the transfer length increases with increasing contact length up to a certain point where the contact length is large enough for $L_{T,FT}$ coincides with $L_{T,TLM}$. From that point onward, the length of the contact is too large for the current density drop to be significant.

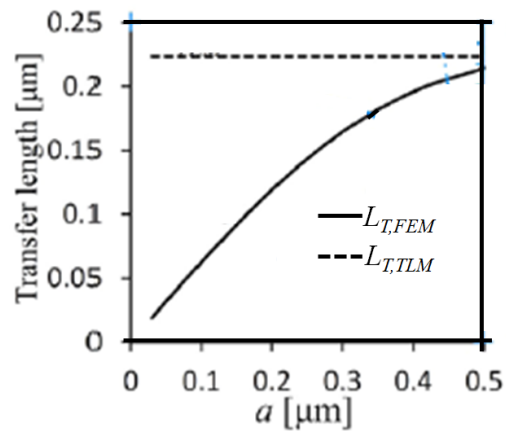
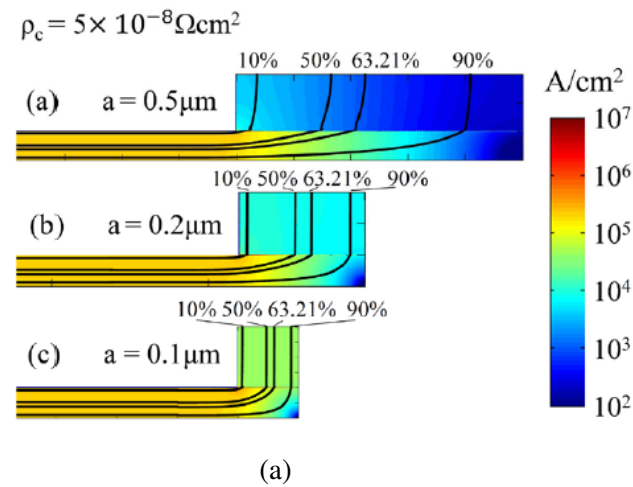
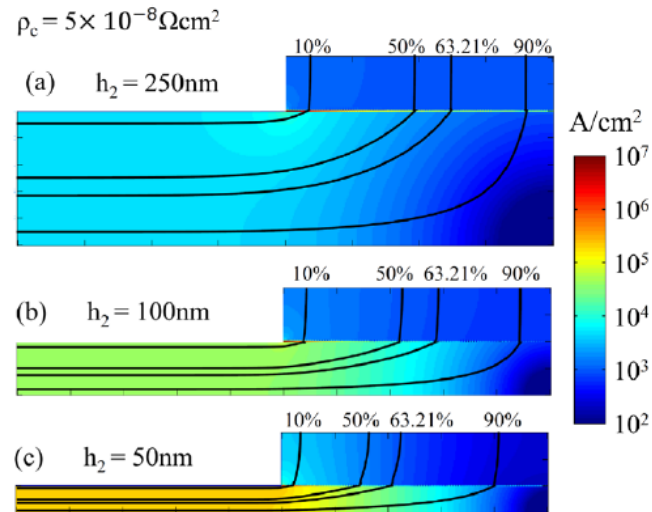


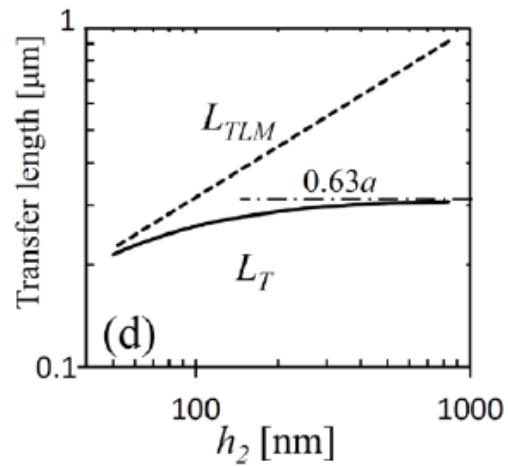
Figure 5.8: (a) Current density distribution on changing contact length (a) from the exact field solution model. (b) Transfer length as a function of contact length, $a(\mu\text{m})$ [25].

5.6.3 Changing Contact Height

The effect of varying the height of the conducting region, h_2 was also modeled and are shown in Figure 5.9. As h_2 decreases, there is significantly more current crowding in the conducting layer. When h_2 is small, $L_{T,FT}$ follows closely with $L_{T,TLM}$ as the TLM model is reliable when only when the length of the conducting layer $h_2 \rightarrow 0$. $L_{T,FT}$ increases with h_2 till it reaches a constant value of 0.63 times the length of the contact due to the fringing field being determined by the smaller of the dimensions in the contact constriction corner [23].



(a)



(b)

Figure 5.9: (a) Current density distribution on changing conducting layer (h_2) from the exact field solution model. (b) Transfer length as a function of height of conducting layer (h_2) [25].

Chapter 6

Fabrication of TLM Structures

Transmission Line Measurement (TLM) structures can be fabricated based on lithographic patterning, etch, deposition and thermal treatment processes. Lithographic patterning is carried out through a mask with predefined levels for MESA isolation, contact cut and metal etch. Two masks were designed for the project. In the first mask, the three levels had TLM patterns where the length was kept constant and TLM width was varied. The layout is shown in Figure 6.1. It included TLM structures that could be tested through the manual test bench or through the automatic probe station. This mask was fabricated using e-beam lithography at RIT using the MEBES mask-making tool. The second mask design shown in Figure 6.2 predominantly included the scaled TLM structures and TLM of changing width and length. It also included circular TLM (CTLM) and 3-D TLM structures that could be used for future research. This mask was fabricated at a commercial site PhotoMask PORTAL™.

A standard process flow is followed for all TLM fabrication steps until the metal deposition. Depending upon type of metal and use of silicides, the process is then altered based on the silicidation reaction or annealing (sinter) for intimate contact formation. The generic process flow for TLM formation until the metal deposition step is described in Figure 6.3. Detailed process flow description is provided with process recipes in Appendix A.

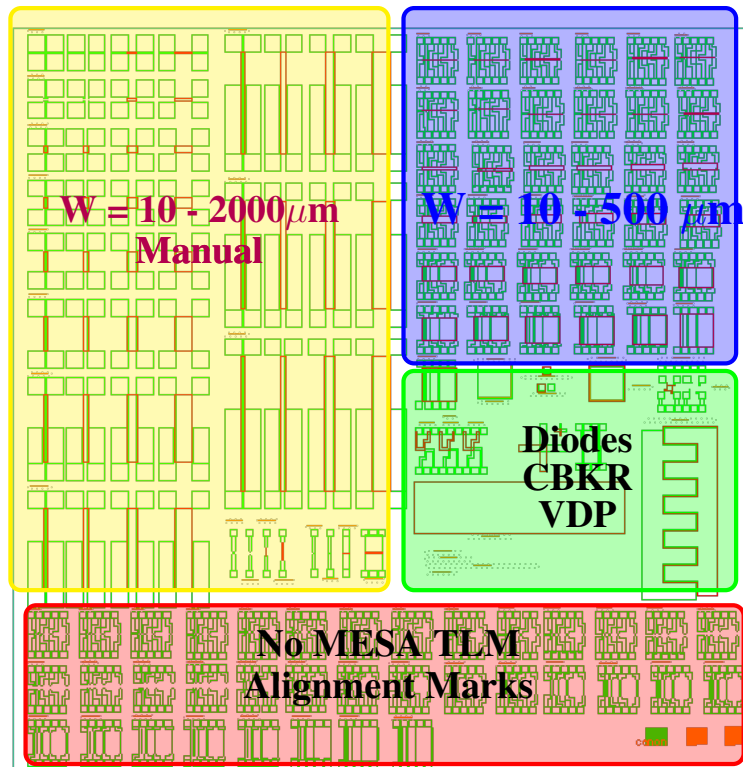


Figure 6.1: Mask layout for constant TLM length and different widths.

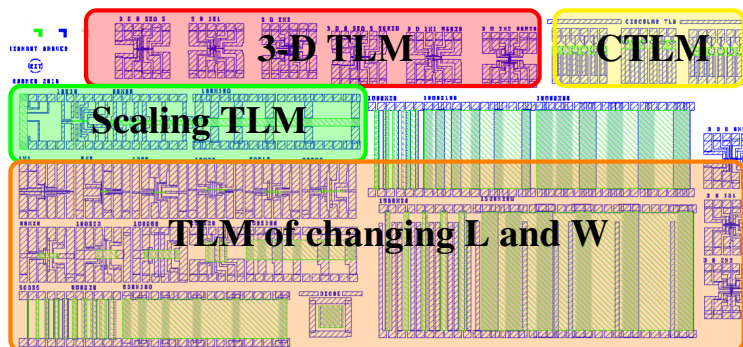


Figure 6.2: Mask layout for constant TLM width and different lengths.

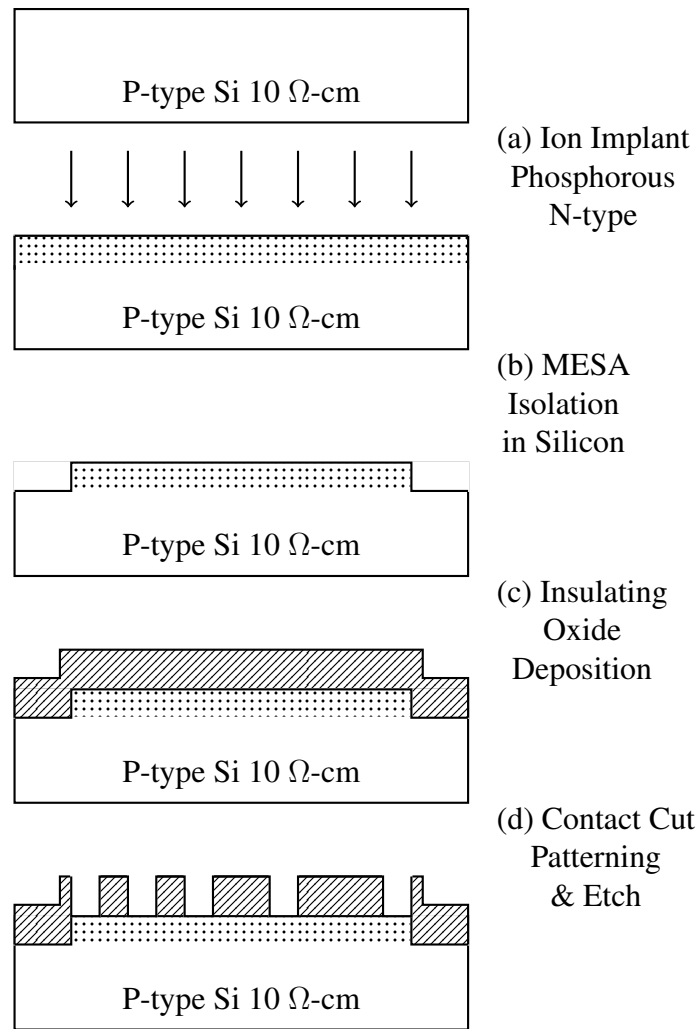


Figure 6.3: TLM fabrication process flow.

6.1 Implant Schemes for Target R_{SH}

In this project, two different design spaces of sheet resistance or R_{SH} were fabricated. The two values of R_{SH} were used to replicated those most commonly seen in real world applications such as silicon photovoltaics and integrated circuits. Low values of the sheet resistance about 10 - 50 $\Omega/sq.$ were comparable to those in silicon photovoltaics and higher values 800 - 1200 $\Omega/sq.$. These values of sheet resistances were obtained through methods of ion implantation and spin-on-doping by light or heavy n-type Phosphorous doping.

Process development for the target R_{SH} was carried out through picking out dose and energy parameters and carrying out process simulations in ATHENA SUPREMTM. For spin-on-doped wafers, the process was simulated through the use of a sacrificial heavily doped oxide layer and diffused into the silicon. The parameters for the target values of R_{SH} through ion implantation are described in Table 6.1 below.

Contact Metal	Dose (cm^{-3})	Energy (keV)	Target R_{SH} ($\Omega/\text{sq.}$)	Meas. R_{SH} ($\Omega/\text{sq.}$)
1 - Al	2×10^{15}	50	50	44.6
2 - Al	2×10^{13}	50	1000	800
3 - TiSi_2	2×10^{15}	50	50	44.6
4 - TiSi_2	2×10^{13}	50	1000	800
5 - NiSi	2×10^{15}	50	50	44.6
6 - NiSi	2×10^{13}	50	1000	800

Table 6.1: Dose and Energy implant parameters for target values of R_{SH} .

The simulations were carried out in ATHENA SUPREMTM and the simulation code is provided in the Appendix B. The implant profiles were used to extract the junction depth or x_j (μm). The x_j directly relates to the thickness of the conducting doped region. The simulated values were used as the basis of generating the target values of R_{SH} in the experiment. Ion implantation using the Varian 350D Implanter through a 30 nm screening oxide was carried with the appropriate dose and energy values from Table 6.1. The screening oxide was to prevent non-uniform channeling across the wafer. The wafers were then annealed in a N_2 ambient at 1000°C to drive in and activate the dopants. The screening oxide was then stripped in a 5.2:1 Buffered Oxide Etch (BOE) solution and inspected. CDE Res Map was used to measure the R_{SH} values. The experimental were not exactly the same as the simulated values but within the range of differentiability between low and high R_{SH} . The experimental values are also recorded in Table 6.1.

Phosphorous doped P509 spin-on-dopant by Filmtronics was used as the source for the spin-on-doped wafers. The process for doping the wafers using this method is summarized

below.

- Dispense 2ml of solution on wafer.
- Ramp for 3 seconds at 500 rpm.
- Spin at 3000rpm for 30 seconds
- Bake on hot-plate for 10 minutes at 200°C
- Drive-in using recipe 325 (see Appendix)
- Strip baked dopant in 5.2:1 HF BOE for 5 minutes.
- Measure R_{SH}

The measured values of R_{SH} were consistent and about $10 \Omega/sq.$.

6.2 Aluminum TLM Process Flow

The process for fabricating Transmission Line Measurement structures for aluminum is described as follows. All the steps are the same until part (d) of Figure 6.3. The steps following involve Aluminum sputter deposition using the CVC601 sputter, patterning using a pre-defined mask level using the ASML stepper and etch to form contacts with bond pads using LAM4600 Rainbow etcher. A brief description is shown in Figure 6.4.

A sintering process is carried out at 450°C to get rid of a native oxide between metal-semiconductor interface and reduce the contact resistance.

6.3 NiSi TLM Process Flow

NiSi metal-semiconductor contacts can be formed by a two-step self aligned process discussed in chapter 4. It involves a sputter deposition of Ni using the P5000 deposition tool

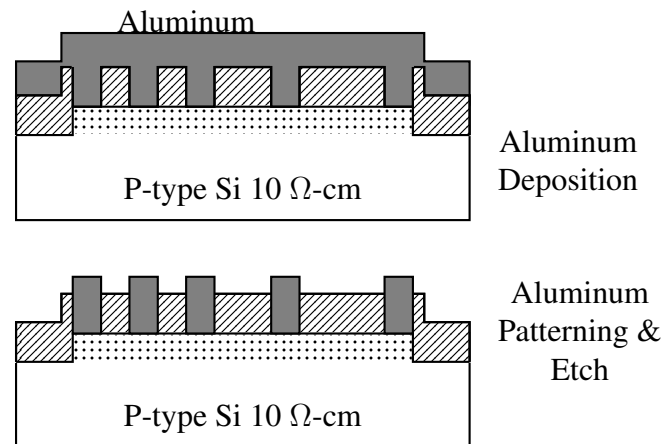


Figure 6.4: Aluminum TLM formation

on the substrate patterned with contact cut openings. The Ni is then silicided through a Rapid Thermal Annealing (RTA) in the AG 610A RTA process. Nickel Silicide is formed in the contact cut openings where the Ni is in direct contact with the silicon. The unreacted Ni is then removed using an etch chemistry mixture of sulphuric acid (H_2SO_4) and hydrogen peroxide (H_2O_2). Aluminum can then be deposited on the NiSi contacts to form bond pads.

6.4 TiSi_2 TLM Process Flow

A similar process to NiSi formation is carried out for the TiSi_2 formation. The only difference is that there is a two-step RTP process involved that converts the high resistive C49- TiSi_2 phase to low resistive C54- TiSi_2 phase.

6.5 Testing of Fabricated TLM Structures

The fabricated TLM structures were tested using the HP4145 test station using the ICS metrics software. 4 point probe I-V measurement was carried out at each resistive test

structure by sweeping voltage from 0-2 Volts and measuring the current across each resistor. This was used to generate I-V curves for each specific resistor with different spacings for the TLM test structure.

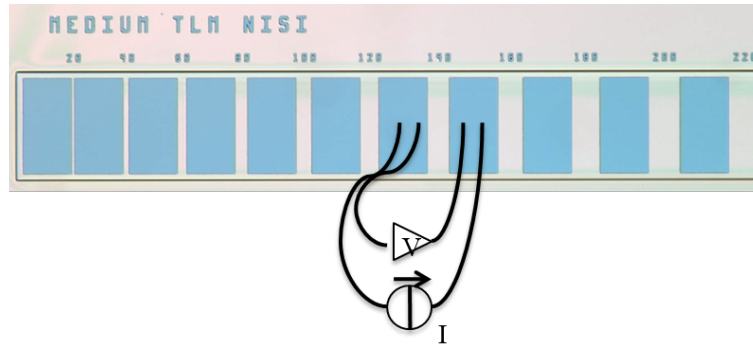


Figure 6.5: Testing of TLM structures

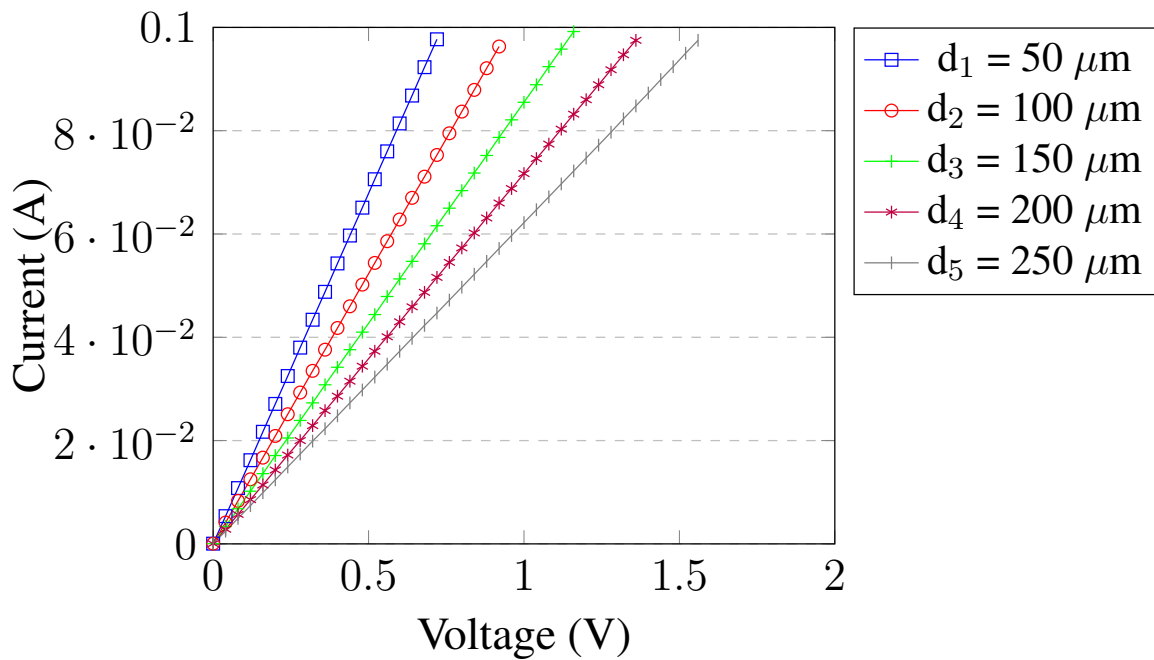


Figure 6.6: I-V plots obtained from measuring resistive contacts from different spacings in the TLM test structure.

The inverse of the slope of each individual curve is the resistance and this resistance is plotted as a function of the pad spacing to extract parameters of transfer length (L_T) and

specific contact resistivity (ρ_c) similar to one observed in Figure 4.3. The extracted L_T is used to calculate the ρ_c from Equation 5.14 using know parameters of W and L. The example of Figure 6.6 involved contacts of Aluminum metal fabricated on heavily doped Silicon of underlying sheet resistance R_{SH} of $50 \Omega/sq.$.

Chapter 7

TLM Structure Optimization

In order to accurately extract the specific contact resistivity from Transmission Line Measurement (TLM) structures, the TLM geometries must be chosen to provide the least amount of error in measurement. These geometries need to also be optimized based on contact material as well as resistive properties of the underlying material to which the contact is made. In other words, the TLM geometries need to be optimized based on sheet resistance of the underlying doped region for a particular semiconductor application and the specific contact resistance of the metal used to make the contact. Optimization of TLM geometries essentially relates to TLM width optimization as we already discussed the choice of length for accurate ρ_c extraction in Chapter 3.

7.1 Optimization Through Error Analysis

Error in the Transmission Line Measurement (TLM) method can be classified into two main types - Random Error and Systematic Error. Random error measures the difference between the mean determined from a large number of trials and a single measurement of the parameter in consideration. Systematic Error is a consistent shift of means of a parameter that cannot be reduced by taking a large number of trials. In this paper, only systematic error was optimized due to ease of calculation and order of importance. The fundamental

variables of the TLM procedure, the total resistance (R), pad spacing (d) and pad width (W) had systematic errors δR , δd and δW associated to them due to errors in measurement. The procedure for evaluating the general error propagation and its contributions to the specific contact resistivity and sheet resistance can be described. The general error in specific contact resistivity and sheet resistance is given by $\Delta\rho_c$ and ΔR_{SH} respectively. A master equation based on Equation (5.1) can be written as below.

$$R = A + Bd \quad (7.1)$$

Where

$$A = 2R_C \quad (7.2)$$

$$B = \frac{R_{SH}}{W} \quad (7.3)$$

$\Delta\rho_c$ and ΔR_{SH} can be expressed in terms of errors in A and B, ΔA and ΔB which in turn can be expressed as uncertainties in the measured parameters ΔR , Δd and ΔW . The expression for ρ_c in the long contact limit can be written in terms of A and B using Equations (6.2) and (6.3) [20].

$$\rho_c = \frac{WA^2}{4B} \quad (7.4)$$

This equation is extremely important as it can be used to determine $\Delta\rho_c$ in terms of error contributions from measured parameters. By differentiating Equation (6.4), the uncertainty in ρ_c can be derived as.

$$\begin{aligned}\Delta\rho_c &\simeq \left|\frac{\delta\rho_c}{\delta A}\right|\Delta A + \left|\frac{\delta\rho_c}{\delta B}\right|\Delta B + \left|\frac{\delta\rho_c}{\delta W}\right|\Delta W \\ &= \left(\frac{WA}{2B}\right)\Delta A + \left(\frac{WA^2}{4B^2}\right)\Delta B + \left(\frac{A^2}{4B}\right)\Delta W\end{aligned}\quad (7.5)$$

The relative uncertainty in ρ_c can therefore be given by.

$$\frac{\Delta\rho_c}{\rho_c} \simeq 2\left(\frac{\Delta A}{A}\right) + \frac{\Delta B}{B} + \frac{\Delta W}{W}\quad (7.6)$$

The relative uncertainty of the sheet resistance (ΔR_{SH}) can be derived in a similar manner and is given by.

$$\frac{\Delta R_{SH}}{R_{SH}} \simeq \frac{\Delta B}{B} + \frac{\Delta W}{W}\quad (7.7)$$

The changes in A and B caused due δR and δd can be described in the TLM extraction plot of differential resistance versus pad spacing plot as shown in the figure below.

For a change in R, i.e. δR , the slope of the plot remains the same and the vertical intercept shifts δR .

$$\delta B|_{\delta R} = 0\quad (7.8)$$

$$\delta A|_{\delta R} = \delta R\quad (7.9)$$

Similarly, change in d, i.e. δd does not change the slope but results in the change of the vertical intercept.

$$\delta B|_{\delta d} = 0\quad (7.10)$$

$$\delta A|_{\delta d} = B\delta d\quad (7.11)$$

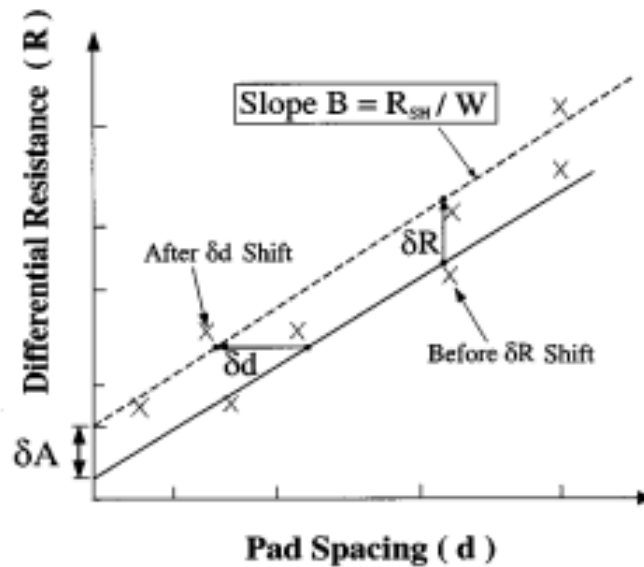


Figure 7.1: Depiction of systematic error through δR or δd on ρ_c extraction through the TLM method [20].

By taking partial derivatives of Equation (6.4) and $A = 2\sqrt{\rho_c R_{SH}}/W$ with respect to W , we get

$$\delta B|_{\delta W} = \left(\frac{B}{W}\right)\delta W \quad (7.12)$$

$$\delta A|_{\delta W} = \left(\frac{A}{W}\right)\delta W \quad (7.13)$$

By substituting the above two equations in Equation (6.6) and (6.7), the total relative uncertainty in the specific contact resistivity due to systematic error is given by Equation (6.14) below.

$$\frac{\delta \rho_c}{\rho_c} = \left(\frac{W}{\sqrt{\rho_c R_{SH}}}\right)\delta R + \left(\sqrt{\frac{R_{SH}}{\rho_c}}\right)\delta d + \left(\frac{4}{W}\right)\delta W \quad (7.14)$$

Similarly, the total relative uncertainty due to systematic error in the sheet resistance is

given by.

$$\frac{\delta R_{SH}}{R_{SH}} = \left(\frac{2}{W} \right) \delta W \quad (7.15)$$

Since the systematic error is more significant, its optimization is more important when compared to the random error. The values of R_{SH} and W which yield minimum uncertainty in ρ_c can be derived from partial derivatives of Equation (6.14) with respect to R_{SH} and W , and setting them equal to zero. This gives us the equation for the optimum width W_{opt} .

$$W_{opt} = \sqrt{4\sqrt{\rho_c R_{SH}} \left(\frac{\delta W}{\delta R} \right)} \quad (7.16)$$

Simulations of the optimum widths can be carried out for application specific ranges of values of R_{SH} and ρ_c . δR and δW are chosen with respect to anticipated error in experimental values where $\delta R = 0.2\Omega$ and $\delta W = 1.5 \mu m$. A contour map of the systematic error optimization can be generated with values of optimum TLM width W_{opt} for each particular combination of R_{SH} and ρ_c .

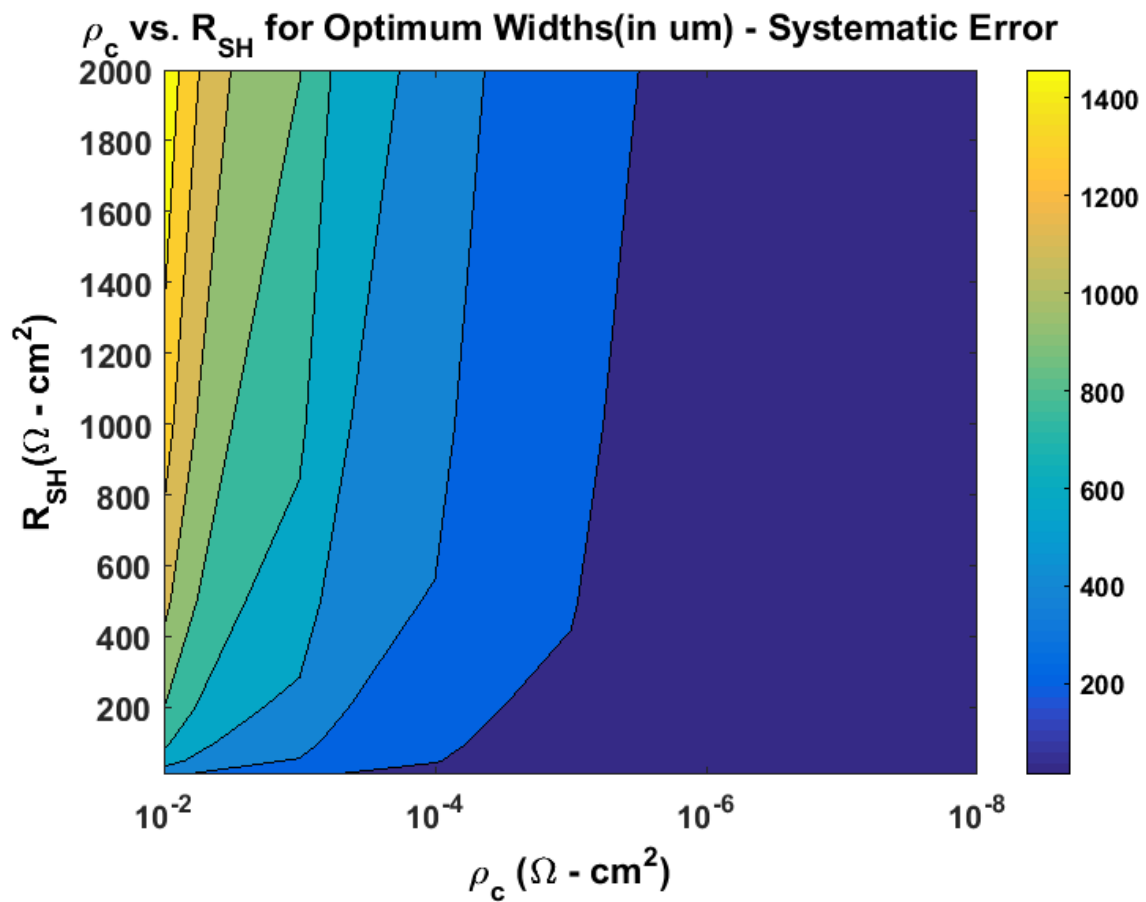


Figure 7.2: Contour map of W_{opt} for application specific ρ_c and R_{SH} .

Chapter 8

Results and Discussion

8.1 Optimization Results

The theory of TLM optimization is described in detail in chapter 6. As mentioned in the chapter, the systematic error optimization of the TLM width can be carried out. A contour map of the optimum width calculated for least relative systematic uncertainty can be generated for application specific values of ρ_c and R_{SH} .

Figure 8.1 is the same contour plot as in Chapter 7. The particular regions of specific contact resistivity and sheet resistance have an optimum value of TLM width W_{opt} that provides the least amount of systematic error in measurement. It can be observed that for larger values of R_{SH} and lower values of ρ_c , the optimum width is in the range of about 800-1200 μm . For lower values of R_{SH} and higher values of ρ_c , the optimum width is clearly below 200 μm .

TLM test structures were fabricated with different contact metals and underlying sheet resistivities of the conducting regions and tested. The relative uncertainty due to systematic error in the specific contact resistivity was calculated for each TLM structure of different contact width. The TLM width that had the least relative uncertainty due to systematic error was the optimum width. Equation 6.14 was used for the calculation of the error in

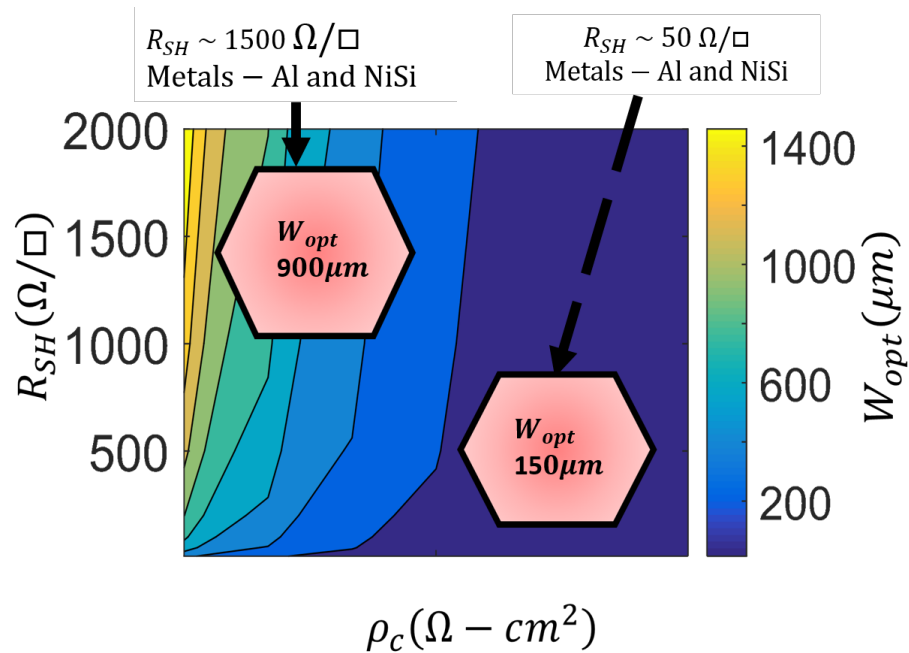


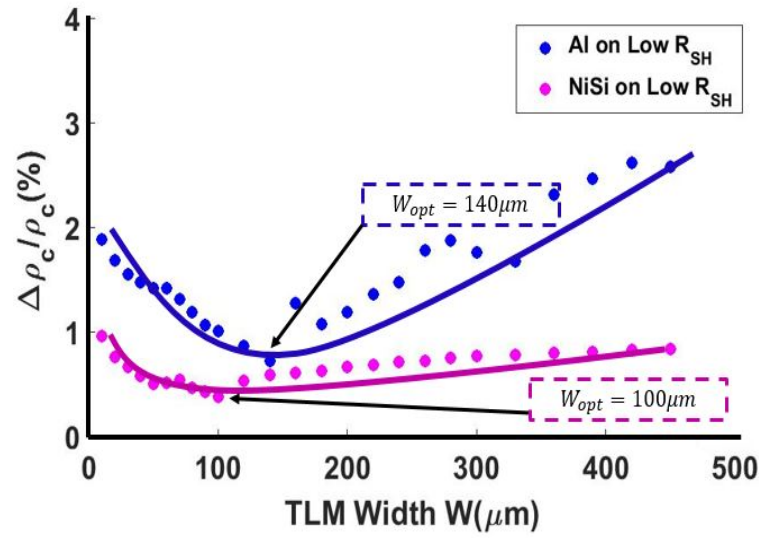
Figure 8.1: Contour plot of the systematic error optimization for application specific values of ρ_c and R_{SH} .

measurement.

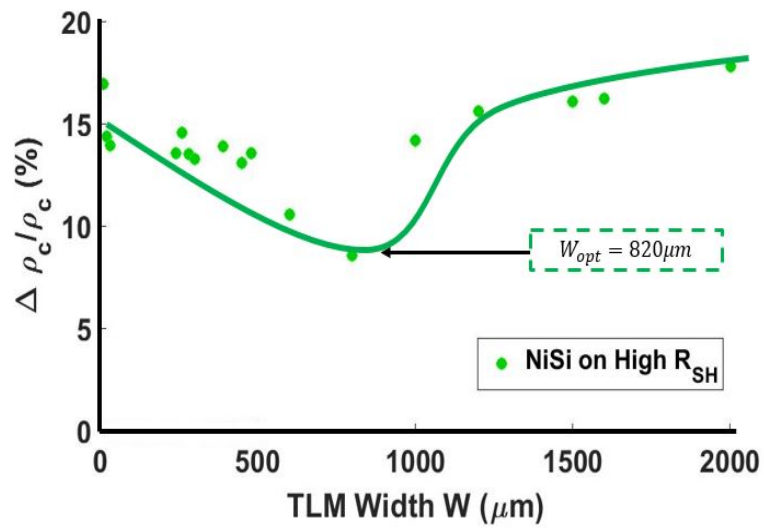
Figure 8.2 shows the values obtained from the calculation of relative uncertainty due to systematic error from the measurement of TLM structures of different lengths. The optimum width can be observed as the minima of the curve as the error in measurement is the least for this particular width of the TLM structure. In the above structures tested, the value of the TLM length was kept at a constant of $10 \mu\text{m}$. The values of δd , δR and δW were $0.5 \mu\text{m}$, 0.2Ω and $1.5 \mu\text{m}$ respectively.

In another experiment, the width of the TLM was kept constant and the length was varied. It was interesting to see that an optimum length could also be found for the different cases under experimentation.

Figure 8.3 shows the relative uncertainty due to systematic error in ρ_c upon keeping the TLM width constant and on changing TLM length. It can be observed that as the TLM length decreases, the uncertainty in measurement of ρ_c is significantly higher. It



(a)



(b)

Figure 8.2: Relative uncertainty due to systematic error as a function of TLM width for (a) low and (b) high R_{SH} using Al and NiSi contact metals.

decreases to an optimum value upon increasing the TLM length and tends to increase again for larger values. The relative uncertainty is also higher for TLM structures fabricated on a conducting layer of higher sheet resistance R_{SH} .

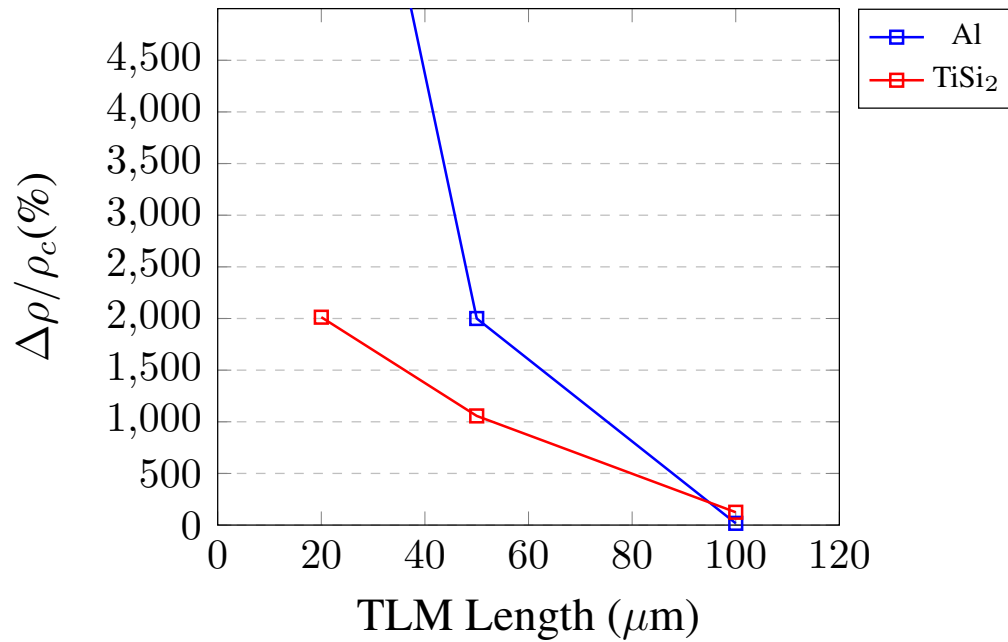


Figure 8.3: Relative uncertainty due to systematic error in specific contact resistivity (ρ_c) as a function of TLM length (L , μm) for $R_{SH} = 1000 \Omega$ and $W = 100\mu\text{m}$.

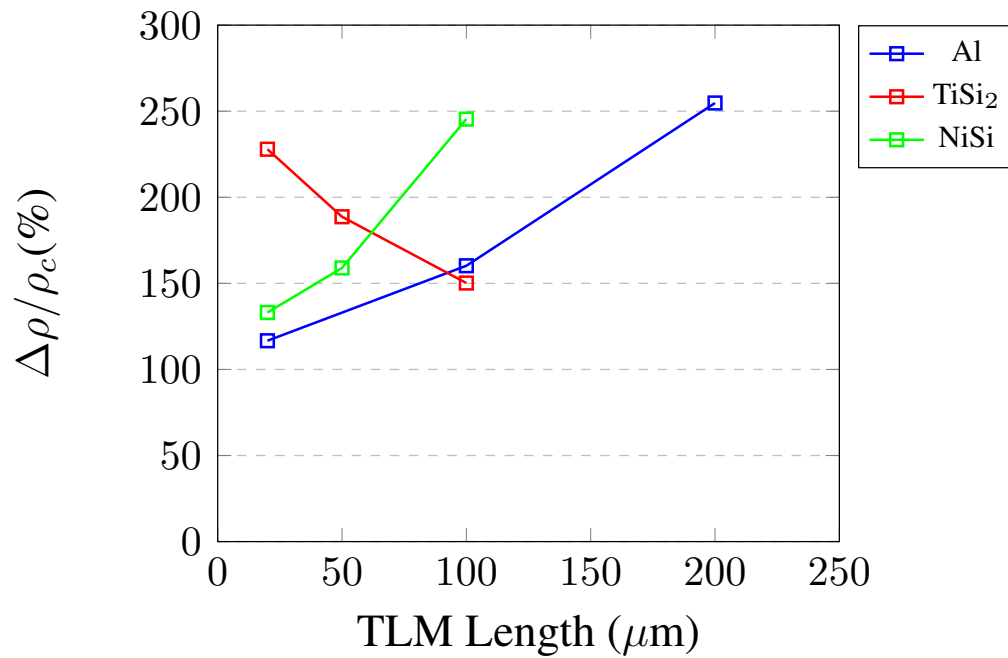


Figure 8.4: Relative uncertainty due to systematic error in specific contact resistivity (ρ_c) as a function of TLM length (L , μm) for $R_{SH} = 50 \Omega$ and constant width $W = 100\mu\text{m}$.

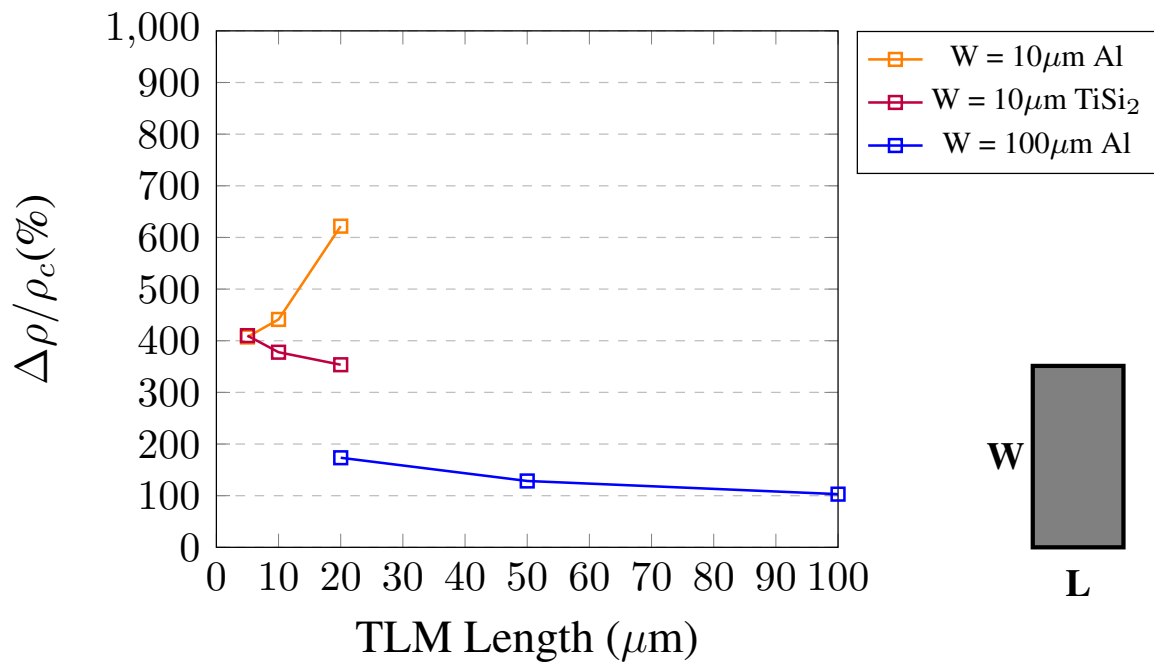


Figure 8.5: Relative uncertainty due to systematic error in specific contact resistivity (ρ_c) as a function of TLM length (L , μm) for $R_{SH} = 10 \Omega$.

A similar trend was observed for the case of values of low R_{SH} as seen in Figure 8.4, only difference being that the values of the relative uncertainty in ρ_c were significantly lower than that obtained from TLM structures with a highly resistive conducting layer. Figure 8.5 also showed higher values of the relative uncertainty indicating that there also exists optimum values of R_{SH} for which there is least amount of systematic error in measurement. This is helpful for optimizing TLM length and width (which gives similar results, Figure 8.2) in order to obtain an optimized design space for applications with a particular R_{SH} .

These results are interesting as it was earlier assumed that the TLM length has no impact on the relative uncertainty due to systematic error. The most probably cause can be attributed to the use of the approximated formula used in the derivation of the equation of the relative uncertainties and optimum widths. If the general TLM formula is used in case of the long contact approximation, the TLM length can be taken into account due to the

hyperbolic dependence of L . As no optimization was carried out for the TLM length, the experimental values could not be compared to any equation or model.

8.2 TLM Width and Transfer Length

Transmission Line Measurement (TLM) structures with a fixed contact length (L) and changing width (W) were fabricated with different contact metals and sheet resistances of the underlying layer. The TLM widths were varied from $10\ \mu\text{m}$ to $2000\ \mu\text{m}$. Upon measurement of the fabricated structures, a trend between the transfer length (L_T or $L_{T,TLM}$) and TLM width dimension was observed.

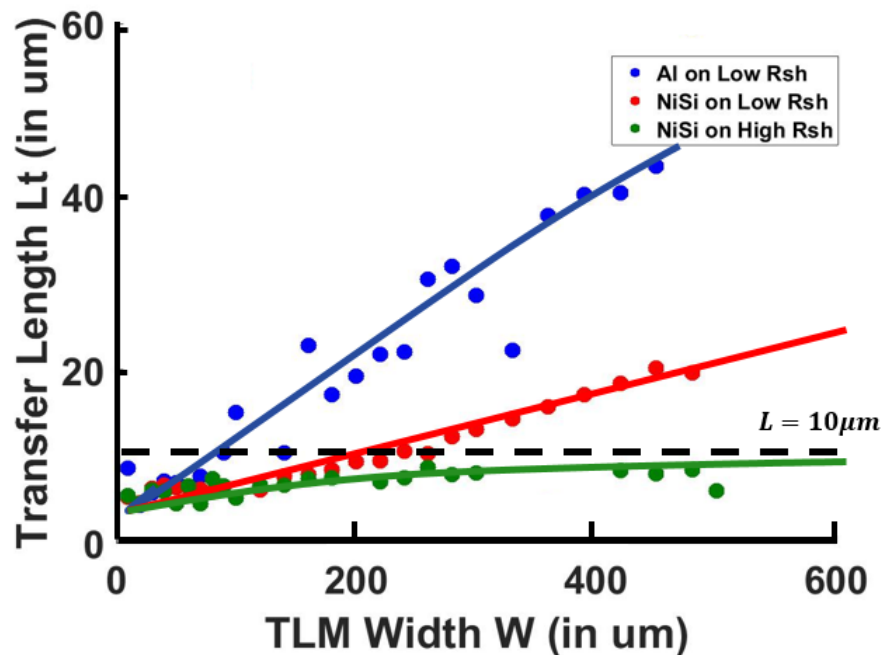


Figure 8.6: Transfer Length as a function of TLM width (W , μm).

It can be seen from Figure 8.6 that larger values of TLM width seem to have longer transfer lengths. This can be attributed to the larger effect of the fringing field at the edges of the contact. This means that current has to flow a larger distance around and under the

contact to get through to the metal. This result was particularly interesting as it has been historically understood that the TLM width has no impact on the transfer length as the flow of current is perpendicular to its direction.

8.3 TLM Design Length and Transfer Length

The impact of changing the TLM length on the extracted transfer length was also studied for a value of constant TLM width. The TLM width was kept constant at $100\ \mu\text{m}$ and the TLM length was varied from $20\ \mu\text{m}$ to $100\ \mu\text{m}$. The results obtained were similar to those observed by scaling TLM dimensions as well as constant length and varying width and are observed in Figure 8.7.

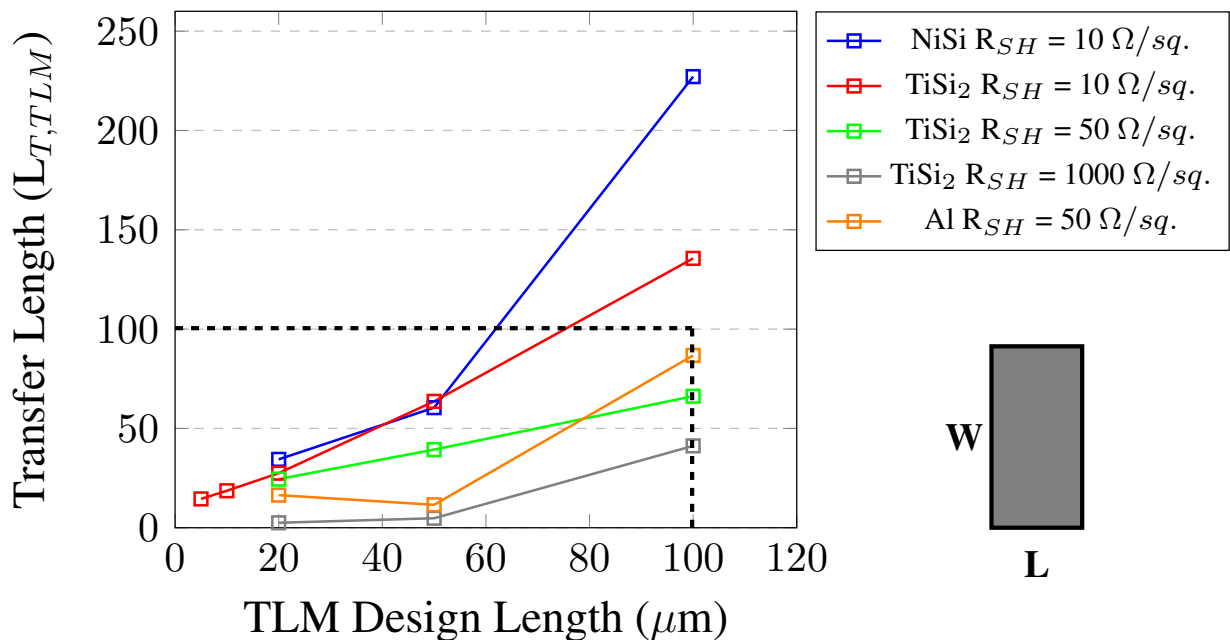


Figure 8.7: Dependence of transfer length on the length of TLM at constant width.

Since the width was kept a constant at $W = 100\ \mu\text{m}$ and the length for some structures was $100\ \mu\text{m}$, the observed transfer length was greater the length of the contact in some cases. It can be observed that the values of the transfer length extracted within the dotted

lines of the contact dimensions are true values whereas those greater than the those true dimensions are fictitious values. The TLM model does not work for those extracted values and other models need to be used to understand this behavior.

8.4 TLM Scaling

In order to understand the variation of transfer length with changing TLM contact dimensions, incrementally scaled TLM structures were fabricated. All dimensions such as the length (L), width (W) and spacings d_1 , d_2 , d_3 etc. were scaled together. For example, a for a structure with a length of $10\mu\text{m}$, width of $10\mu\text{m}$ and d_1 , d_2 , d_3 , d_4 and d_5 of 10, 20, 30, 40 and $50\mu\text{m}$ respectively had 5x scaled structures of length of $50\mu\text{m}$, width of $50\mu\text{m}$ and d_1 , d_2 , d_3 , d_4 and d_5 of 50, 100, 150, 200 and $250\mu\text{m}$ and 10x scaled structures of length of $100\mu\text{m}$, width of $100\mu\text{m}$ and d_1 , d_2 , d_3 , d_4 and d_5 of 100, 200, 300, 400 and $500\mu\text{m}$.

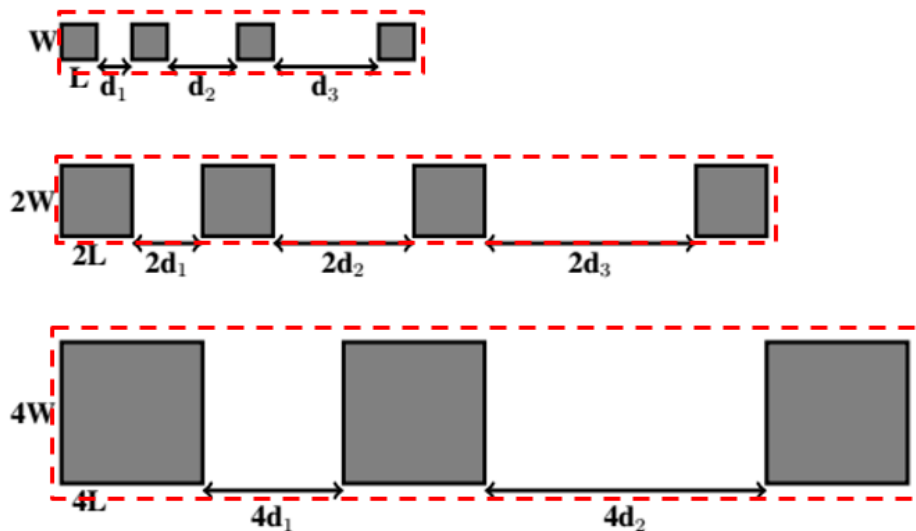


Figure 8.8: Scaled TLM contact structures with 1x, 2x and 4x scaling.

It can be observed that the transfer length scales proportionally with the TLM dimensions. The plots seen in Figure 8.9 are very close to linearity which shows that the specific

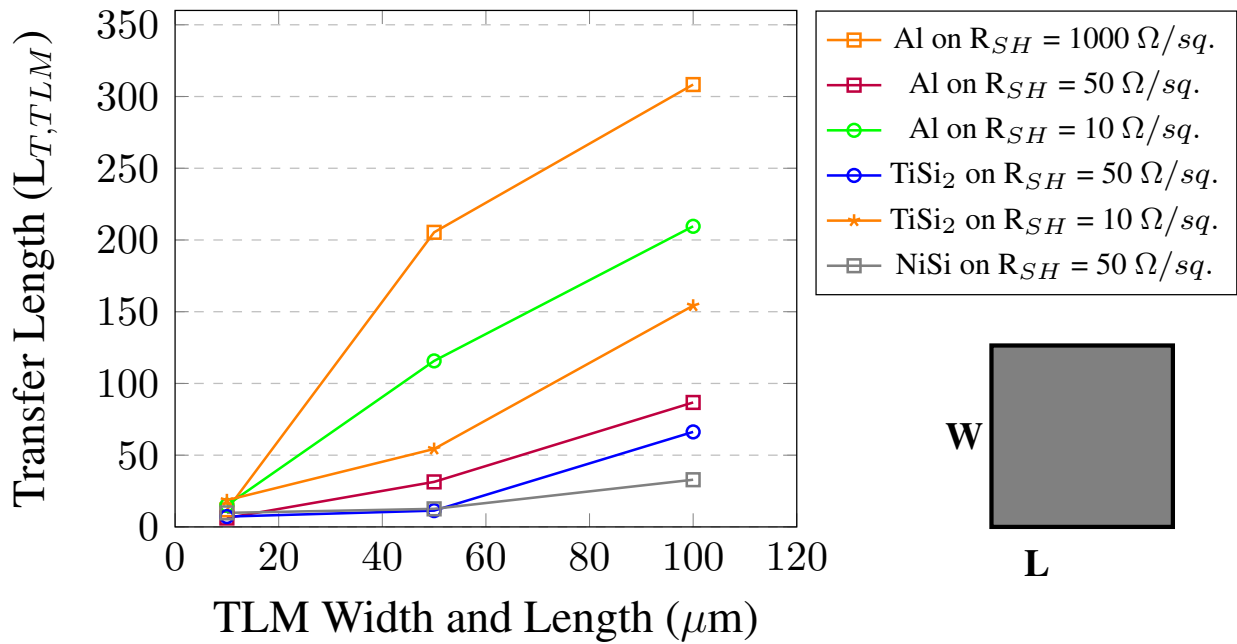


Figure 8.9: Scaling effect of TLM dimensions on Transfer Length.

contact resistivity does seem to be affected by the contact dimensions. Upon increasing the length, width and spacing between the contacts, the transfer length extracted from the measurement of the TLM structures increases accordingly. This relation is similar to one we observe in realistic applications where TLM geometries vary such as high values of ρ_c for photovoltaic applications with larger TLM geometries and low ρ_c for integrated circuit applications with smaller TLM geometries. The standard TLM model is not valid once the extracted TLM transfer length is greater than actual contact geometries.

8.5 Modeling Results

In order to better understand the behavior of the flow of the current under these contacts experimental parameters were modeled using techniques discussed in Chapter 5. These were helpful to explain the trends observed in the variation of the transfer length due to contact geometry.

8.5.1 Fourier Series Analysis Modeling

As discussed in Chapter 5, the Fourier Series Analysis can be used to extract an exact field solution giving meaningful insights of the current density distribution, current flow patterns, contact resistance that consists of the interface resistance and the constriction (spreading resistance) due to current crowding [25]. The structure used for the simulation of the model is the same as Figure 5.6 and is shown again below.

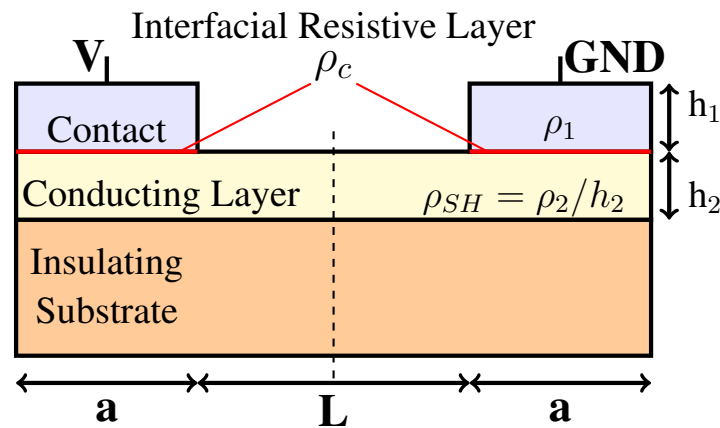


Figure 8.10: Two contact structure for Fourier Series Analysis simulations.

Figure 8.9 describes two contacts that are placed on top of a conducting layer. This conducting layer is laid on top of an insulating substrate. The contacts are of resistivity ρ_1 , height of h_1 and the length of the contact is a . The conducting layer has a height of h_2 and a resistivity of ρ_{SH} . The spacing between the two contacts is given by L . An interfacial layer, which is infinitesimally small is in between the contacts and the conducting layer, it has a specific contact resistivity (or specific interfacial resistivity) denoted by ρ_c . When a bias is applied between the two contacts, current flows from one contact to the other through the conducting layer.

Realistic application specific values of specific contact resistivity or interfacial resistivity ρ_c , contact length a , conducting layer resistivity ρ_{SH} , and conducting layer height h_2 were provided to Dr. Peng Zhang at the University of Michigan to simulate to see trends

on the transfer length using codes based on Fourier series analysis. Graphs for variation of the transfer lengths $L_{T,TLM}$ and $L_{T,FT}$ with respect to the specific contact resistivity ρ_c can be plotted for the different values of ρ_{SH} and h_2 .

For a fixed value of contact length $a = 10\mu\text{m}$, the resistivity of the conducting layer ρ_{SH} is changed based on expected values of the junction depth (x_j) of a particular dopant and is given values of $50\ \Omega/\text{sq.}$, $1000\ \Omega/\text{sq.}$ and $1500\ \Omega/\text{sq.}$ for corresponding h_2 or x_j values of $0.5\mu\text{m}$, $0.4\mu\text{m}$ and $0.35\mu\text{m}$. The transfer length was calculated using the conventional TLM and the fourier models for realistic values of ρ_c ranging between 10^{-8} and $10^{-2}\ \Omega - \text{cm}^2$.

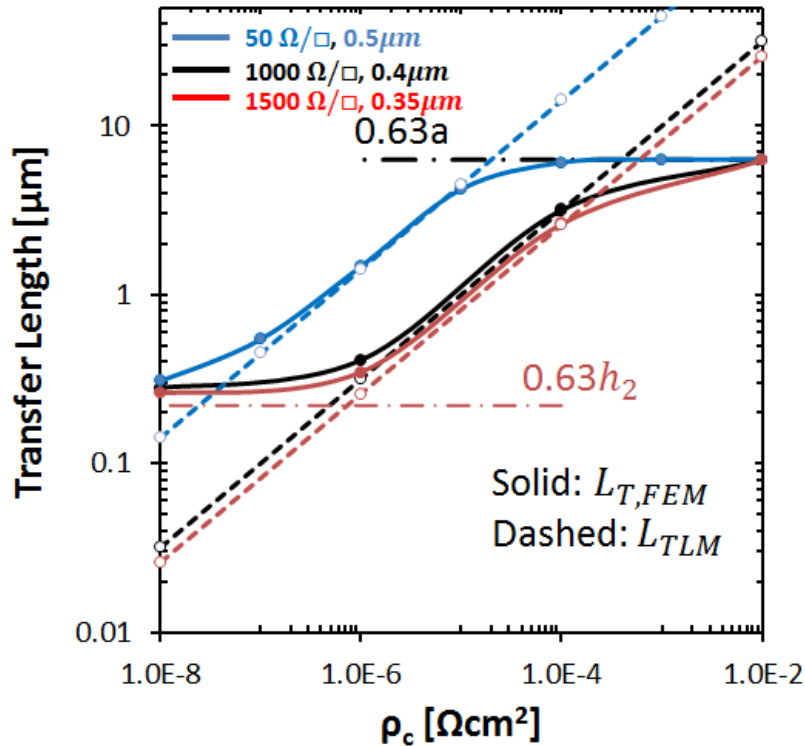


Figure 8.11: Modeled transfer length versus specific contact resistivity for $a = 10\mu\text{m}$.

In Figure 8.10, the solid lines represent the transfer length modeled through the exact field solution ($L_{T,FT}$) and the dashed line is the transfer length evaluated using the conventional TLM model ($L_{T,TLM}$). Different curves are traced for different values of the

resistivity of the underlying layer which is ρ_{SH} in this model. For the conventional TLM model, this would relate to the sheet resistance of the region under the contact R_{SH} . The height of the conduction region h_2 is analogous to the junction depth. It can be observed that the Fourier Analysis and TLM model tend to agree for lower values of ρ_c when ρ_{SH} is lower and h_2 is high. As ρ_{SH} increases and h_2 decreases, the agreement between the Fourier analysis and TLM model shifts towards higher values of ρ_c . It can also be observed that the upper and lower limits of $L_{T,FT}$ are bound by the length of the contact and the height of the conducting layer. This causes the models to diverge for lower and higher values of ρ_c . The saturation of $L_{T,FT}$ for its lower limit is due to the fringing field being attributed to the smaller of the dimensions in the current crowded corners which in this case would happen to be the contact length.

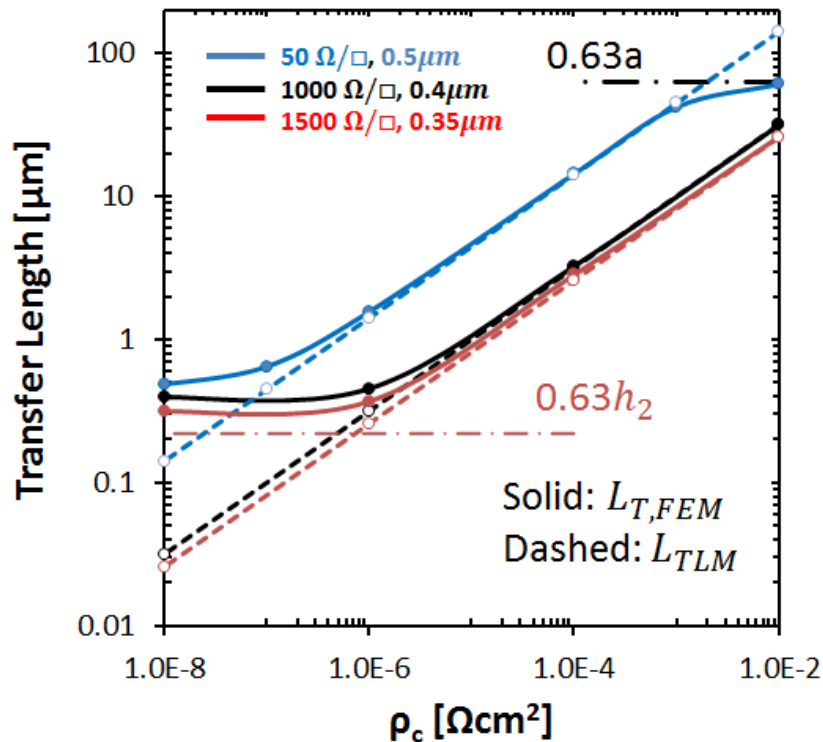


Figure 8.12: Modeled transfer length versus specific contact resistivity for $a = 100\mu\text{m}$.

Figure 8.11 is modeled with the same parameters from Figure 8.10 except the fact that the length of the contact is increased to $100\mu\text{m}$. It can be observed that the agreement between $L_{T,TLM}$ and $L_{T,FT}$ exists for a much wider range of values of ρ_c . For higher values of ρ_{SH} there is very good agreement for larger values of ρ_c and they coincide as the transfer length increases.

The results from these simulations can be very helpful in deciding appropriate TLM contact design geometries for application specific values of R_{SH} and ρ_c . The applicability of the general TLM model can be evaluated based on where the transfer lengths in each of the model coincide. From figures 8.10 and 8.11, the regions of ρ_c where the solid and dashed lines are the same. It was also very interesting to notice that for the values at which the two models agreed, $L_T = 0.4 \times L$. The explanation for this was beyond the scope of this project and is suggested as future work. Therefore, for contact applications of ρ_c smaller than $10^{-6} \Omega\text{-cm}^2$, the exact field solution model can better take into account current constriction effects and gives a more accurate value of ρ_c . This also means the TLM model under estimates the value of the transfer length and it is lower for smaller values of ρ_c which offers an explanation to values for integrated circuit applications observed in literature. This also means that values of ρ_c larger than $10^{-4} \Omega\text{-cm}^2$, transfer length is largely overestimated explaining larger values of ρ_c for silicon photovoltaic applications.

Chapter 9

Conclusions and Future Work

In this project, various methods were explored to understand the reason for inconsistent values of ρ_c observed in literature due to differences in TLM contact dimensions used. Starting from a brief introduction to ohmic contact theory and specific contact resistivity (ρ_c), the different kinds of metal-semiconductor contacts popularly used were explored. The Transmission Line Measurement (TLM) method was then described in detail and the process of determining ρ_c was described. In order to better understand the TLM method, various models like dimensional models, lumped circuit models and exact field solution or fourier transform models were described. The TLM structures were then fabricated based on optimized width values that were designed on a 3-level mask design.

9.1 Conclusions

The error optimization for the TLM widths was confirmed by the experimental results as TLM structures having widths W with the least amount of systematic error in ρ_c could clearly be identified and the experimental values closely matched the ones that were simulated. It was also interestingly observed the for values of constant TLM width and changing length, there appeared to be optimum values of TLM length as well. These values could not be significantly extracted due to lack of experimental data and no optimization had

been carried out on the general TLM formula. Furthermore, there was a dependence of the transfer length L_T on the TLM width when the TLM length was kept constant. As the width was increased, the L_T also increased. A similar trend was observed when the TLM width was kept constant and the TLM length was increased. This was attributed to current crowding and constriction effects of current under the contacts.

The scaled structures were fabricated to confirm the dimensional dependence of L_T and it was observed again that as the length and width of the TLM structures were increased, the transfer length increased accordingly. It was concluded that beyond a certain regime of TLM geometry for a particular application, the general TLM model does not work as the extracted TLM L_T is greater than the length of the contact. To further understand the reason of this behavior, Fourier transform model or the Exact Field Solution model was used. It was observed that the Exact field solution and the general TLM models agreed only for certain values of ρ_c and L_T . This value was only where $L_T = 0.4 \times L$. Below those values, for significantly lower values of ρ_c , the transfer length is underestimated due to current crowding and for larger values of ρ_c , there is an overestimation due to the assumption of current flow equally into the contact.

It was concluded that there is no universal design to determine ρ_c using the TLM method. There is no "one-size-fits-all" geometry and it changes based on application space. The scaling structures confirmed the dependence of TLM geometry on L_T . Figure 9.1 describes this result.

It can be seen from Figure 9.1 that for very low values of ρ_c , L_T is drastically underestimated. Since, lower values of ρ_c are predominantly seen in integrated circuit applications, it could also be said that the TLM method is not an accurate method to determine ρ_c for such applications. The silicon photovoltaics community on the other hand may actually be quoting ρ_c values larger than the true values and must design contact dimensions based projected transfer length values.

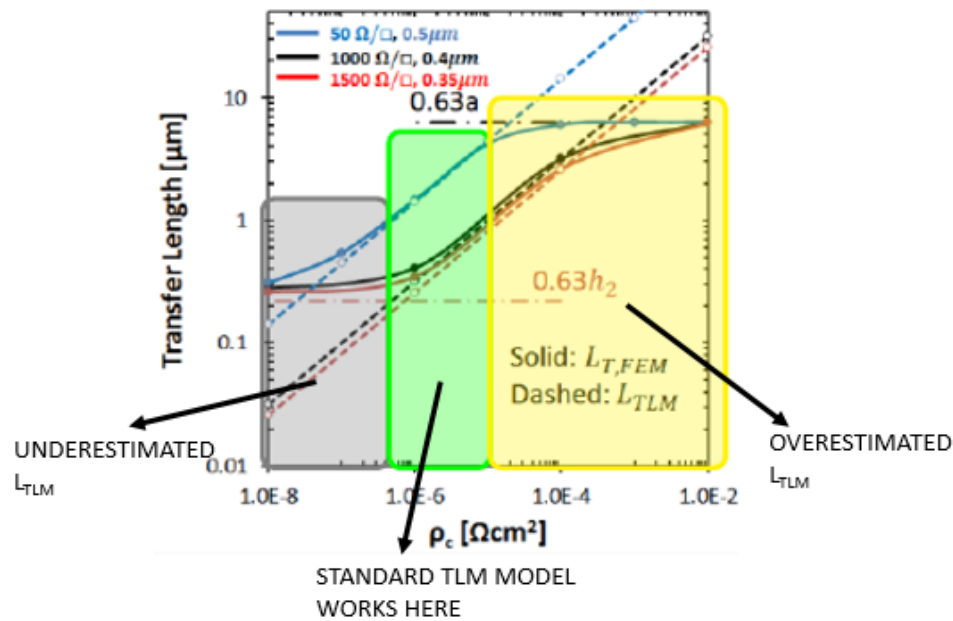


Figure 9.1: Overestimation and Underestimation by the TLM model.

9.2 Future Work

In order to further understand the variation of extracted TLM transfer length and specific contact resistivity on TLM geometries and expand this research, a number of future studies can be suggested extending on this work.

- Carry out TLM optimization of generalized TLM equation that has the coth dependence on L to evaluate values of optimum TLM lengths.
- Develop a database of optimized TLM length and width dimensions that can be used for any particular application of varying sheet resistance of underlying layer.
- Incorporate metal resistivity into L_T determination and TLM dimension optimization.
- Further this research by studying novel contact schemes such as dipole insertion, implanted metal contacts, germanosilicided contacts etc. and discuss the applicability

of the TLM method in such low specific contact resistivity schemes.

- Extend the TLM method to non-planar structures fabricated and closely emulate three dimensional contacts observed in FinFET applications.

...

Bibliography

- [1] Specific contact resistivity versus electron concentration.
- [2] Reduction of base access resistance in algan/gan heterojunction bipolar transistors using gainn base cap layer and selective epitaxial growth. *MRS Online Proceeding*, 892(2):022113, 2006.
- [3] L.J. Chen and Institution of Electrical Engineers. *Silicide Technology for Integrated Circuits*. Iee Materials and Devices Series. Institution of Engineering and Technology, 2004.
- [4] F Deng, RA Johnson, PM Asbeck, SS Lau, WB Dubbelday, T Hsiao, and J Woo. Salicidation process using nisi and its device application. *Journal of applied physics*, 81(12):8047–8051, 1997.
- [5] Evan Franklin, Kean Fong, Keith McIntosh, Andreas Fell, Andrew Blakers, Teng Kho, Daniel Walter, Da Wang, Ngwe Zin, Matthew Stocks, Er-Chien Wang, Nicholas Grant, Yimao Wan, Yang Yang, Xueling Zhang, Zhiqiang Feng, and Pierre J. Verlinden. Design, fabrication and characterisation of a 24.4interdigitated back contact solar cell. *Progress in Photovoltaics: Research and Applications*, 24(4):411–427, 2016. PIP-14-178.R1.
- [6] Andrew M Gabor, Geoffrey Gregory, Adam M Payne, Rob Janoch, Andrew Anselmo, Vijay Yelundur, and Kristopher O Davis. Dependence of solar cell contact resistivity measurements on sample preparation methods. In *43rd IEEE Photovoltaics Specialist Conference*, 2016.
- [7] Kevin Gallacher, P Velha, Douglas J Paul, I MacLaren, Maksym Myronov, and David R Leadley. Ohmic contacts to n-type germanium with low specific contact resistivity. *Applied Physics Letters*, 100(2):022113, 2012.
- [8] A. Goetzberger, J. Knobloch, and B. Voss. *Crystalline Silicon Solar Cells*. Wiley, 1998.

- [9] LASZLO Gutai. Statistical modeling of transmission line model test structures. i. the effect of inhomogeneities on the extracted contact parameters. *IEEE Transactions on Electron Devices*, 37(11):2350–2360, 1990.
- [10] C. Hu. *Modern Semiconductor Devices for Integrated Circuits*. Prentice Hall, 2010.
- [11] Randy W Mann, Larry A Clevenger, Paul D Agnello, and Francis R White. Silicides and local interconnections for high-performance vlsi applications. *IBM Journal of Research and Development*, 39(4):403–417, 1995.
- [12] Thaddeus B Massalski, Hiroaki Okamoto, PR Subramanian, Linda Kacprzak, and William W Scott. *Binary alloy phase diagrams*, volume 1. American Society for Metals Metals Park, OH, 1986.
- [13] Krishna Saraswat. Metal/semiconductor ohmic contacts. 2009.
- [14] Donald Sawdai, Dimitris Pavlidis, and Delong Cui. Enhanced transmission line model structures for accurate resistance evaluation of small-size contacts and for more reliable fabrication. *IEEE Transactions on Electron Devices*, 46(7):1302–1311, 1999.
- [15] Dieter K. Schroder. *Semiconductor Material and Device Characterization*. Wiley-Interscience, 2006.
- [16] N Stavitski, MJH Dal, RAM Wolters, AY Kovalgin, and J Schmitz. Specific contact resistance measurements of metal-semiconductor junctions. 2006.
- [17] Natalie Stavitski. Silicide-to-silicon specific contact resistance characterization. 2009.
- [18] Natalie Stavitski, Johan H Klootwijk, Henk W van Zeijl, Alexey Y Kovalgin, and Rob AM Wolters. Cross-bridge kelvin resistor structures for reliable measurement of low contact resistances and contact interface characterization. *IEEE Transactions on Semiconductor Manufacturing*, 22(1):146–152, 2009.
- [19] Loic Tous. Nickel/copper plated contacts as an alternative to silver screen printing for the front side metallization of industrial high efficiency silicon solar cells (elektrochemisch gedeponeerde nikkel/koper contacten als alternatief voor zilver zeefdruk voor metallisatie van de voorzijde van hoog-efficiënte industriële silicium zonnecellen). 2014.

- [20] Haw-Jye Ueng, David B Janes, and Kevin J Webb. Error analysis leading to design criteria for transmission line model characterization of ohmic contacts. *IEEE transactions on electron devices*, 48(4):758–766, 2001.
- [21] Yewu Wang, Volker Schmidt, Stephan Senz, and Ulrich Gösele. Epitaxial growth of silicon nanowires using an aluminium catalyst. *Nature nanotechnology*, 1(3):186–189, 2006.
- [22] S. Wolf and R.N. Tauber. *Silicon Processing for the VLSI Era: Process technology*. Silicon Processing for the VLSI Era. Lattice Press, 2000.
- [23] Peng Zhang. *Effects of surface roughness on electrical contact, RF heating and field enhancement*. PhD thesis, The University of Michigan, 2012.
- [24] Peng Zhang and Y. Y. Lau. An exact field solution of contact resistance and comparison with the transmission line model. *Applied Physics Letters*, 104(20), 2014.
- [25] Peng Zhang, YY Lau, and RM Gilgenbach. Analysis of current crowding in thin film contacts from exact field solution. *Journal of Physics D: Applied Physics*, 48(47):475501, 2015.

Appendix A

Detailed Process Flow

Starting Material

Bare Si p-type 1-10 Ohms/sq. Init. Resistivity

Zero Level Lithography

ASML Stepper

Zero Etch

Drytek Quad

CHF3 - 50sccm

CF4 - 25 sccm

O2 - 10 sccm

RF - 200W

Pressure - 100mT

Time - 120 seconds

Resist Strip

RCA Clean

Manual RCA Bench

Screening Oxide Growth

Bruce Furnace

LFULL Recipe 250

Target Thickness 250 - 300 Angstroms

Ion Implantation

Varian Ion Implanter

Wafer P1 - Dose 2×10^{13} ; Energy 50keV

Wafer P2 - Dose 2×10^{15} ; Energy 50keV

Wafer P3 - Dose 2×10^{15} ; Energy 50keV

Wafer P4 - Dose 2×10^{15} ; Energy 50keV

Wafer P5 - Dose 2×10^{15} ; Energy 50keV

Wafer P6 - Dose 2×10^{15} ; Energy 50keV

Anneal

Bruce Furnace

LFULL Sub CMOS Anneal Recipe 106

Screening Oxide Etch

5.2:1 BOE Solution

Measure R_{SH}

CDE ResMap

MESA Level Lithography

ASML Stepper

Level 1 - RITTLM2016

MESA Etch

LAM 490

EMCR 613 POLY

Pressure 300mT

RF 150W

O₂ 40 sccm

SF₆ 150 sccm

Resist Strip

GASONICS Aura 1000

TEOS Deposition

AMAT LPCVD P5000

Target thickness - 2000 Angstroms

Contact Cut Lithography

ASML Stepper

Level-2 CC

Contact Cut Etch TRION RIE

Recipe - PVKavya

Time - 350 seconds

Resist Strip

Metal Deposition

CVC601

Aluminum Wafers P1 and P4

Ar flow 20 sccm

Pressure 5mTorr

Power 2000W

Time 1500s

Ti Wafers P2 and P5

Pressure 5 mTorr

Power 750W

Time 300s

PE4400

Ni Wafers P3 and P6

Pressure 8mT

Power 500W

Time 180s

Silicidation

AG 610A RTP

Ti Silicidation Wafers P2 and P5

Recipe FACTISI1.RCP 1 min

Ni Silicidation Wafers P3 and P6

Recipe SISOC550.RCP

Piranha for unreacted metal removal

TiSi₂ Wafers P2 and P5

150 ml H₂SO₄ 300 ml H₂O₂

90 deg 120 seconds

DI Rinse 5 min

Spin-Rinse-Dry

NiSi Wafers P3 and P6

300 ml H₂SO₄ 150 ml H₂O₂

90 deg 300 seconds

DI Rinse 5 min

Spin-Rinse-Dry

Silicidation

AG 610A RTP

Ti₂ Silicidation Wafers P2 and P5

Recipe FACTISI2.RCP 1 min

Piranha for unreacted metal removal

TiSi₂ Wafers P2 and P5

150 ml H₂SO₄ 300 ml H₂O₂

90 deg 120 seconds

DI Rinse 5 min

Spin-Rinse-Dry

Metal Deposition

CVC601

Aluminum Wafers P2, P3, P5 and P6

Ar flow 20 sccm

Pressure 5mTorr

Power 2000W

Time 1500s

Metal Lithography

ASML Stepper

Level3- Metal

Metal Etch

LAM4900 Rainbow Etcher

Recipe 122122

Sinter

Bruce Furnace

Wafers P1 and P4

Recipe LFULL 101

Appendix B

ATHENA code for Implant Simulations

```
go athena
line x loc=0 spac=0.1
line x loc=0.35 spac=0.02
line x loc=1 spac=0.1
#
line y loc=0.00 spac=0.005
line y loc=0.3 spac=0.015
line y loc=0.5 spac=0.02
line y loc=2 spac=0.2
line y loc=5 spac=1
method grid.ox=0.001
# initial wafer
init silicon boron resistivity=10 orientation=100
# implant P
#savefile
structure outfile=Process_Sid.str
# Steam Oxide Growth
```

```
#
method two.dim
diffus time=15 temp=800 f.n2=10
diffus time=10 temp=800 t.final=900 f.o2=5
diffus time=93 temp=900 f.o2=10
diffus time=5 temp=900 f.n2=15
diffus time=20 temp=900 t.final=800 f.n2=10
implant phosphor dose=1.5e13 energy=50 tilt=7
  rotation=45 crystal
diffus time=15 temp=800 f.n2=10
diffus time=10 temp=800 t.final=900 f.n2=10
diffus time=30 temp=900 f.n2=15
diffus time=5 temp=900 f.n2=10
diffus time=20 temp=900 t.final=800 f.n2=10
extract name="ARC" thickness material="SiO~2"
mat.occno=1 x.val=0.45
# deposit TEOS
deposit oxide thick=0.5
#Etch TEOS on half of wafer
#
etch oxide left p1.x=0.5
deposit oxide thick=0.03
implant phosphor dose=2e15 energy=50 tilt=7
rotation=45 crystal
#
etch oxide all
```

```
extract name="Rs3" n.sheet.res material="Silicon"
  mat.occno=1 x.val=0.45 region.occno=1
extract name="xJ3" xj material="Silicon"
  mat.occno=1 x.val=0.45 junc.occno=1
extract name="feildox2" thickness material="SiO~2"
mat.occno=1 x.val=0.2
extract name="Rs2" n.sheet.res material="Silicon"
  mat.occno=1 x.val=0.65 region.occno=1
extract name="xJ2" xj material="Silicon" mat.occno=1
  x.val=0.65 junc.occno=1
extract name="feildox" thickness material="SiO~2"
  mat.occno=1 x.val=0.8
structure outfile=Sid_Process.str
tonyplot Sid_Process.str
quit
RESULTS -
Rs3=49.6841 ohm/square X.val=0.45
EXTRACT> extract name="xJ3" xj material="Silicon"
mat.occno=1 x.val=0.45 junc.occno=1
xJ3=0.463826 um from top of first Silicon layer X.val=0.45
EXTRACT> extract name="feildox2" thickness
material="SiO~2" mat.occno=1 x.val=0.2
Extracted results: N/A
Check cut line and/or selected quantities
EXTRACT>
EXTRACT> #
```

```
EXTRACT> #deposit oxide thick=0.5 c.phosphor=1e21
EXTRACT>
EXTRACT> #diffus time= 20 temp = 900 f.n2 =10
EXTRACT>
EXTRACT> #etch oxide all
EXTRACT> extract name="Rs2" n.sheet.res material="Silicon"
  mat.occno=1 x.val=0.65 region.occno=1
Rs2=1705.91 ohm/square X.val=0.65
EXTRACT> extract name="xJ2" xj material="Silicon"
mat.occno=1 x.val=0.65 junc.occno=1
xJ2=0.368363 um from top of first Silicon layer X.val=0.65
```

...